Title: **A novel Strain-Energy-Density based fatigue criterion accounting for mean stress and plasticity effects on the medium-to-high-cycle uniaxial fatigue strength of plain and notched components**

Authors: **M. Benedetti, F. Berto, L. Le Bone, C. Santus**

DOI Link: https://doi.org/10.1016/j.ijfatigue.2019.105397

A novel Strain-Energy-Density based fatigue criterion accounting for mean stress and plasticity effects on the medium-to-high-cycle uniaxial fatigue strength of plain and notched components

M. Benedetti[a*], F. Berto[b], L. Le Bone[c], C. Santus[c]

[a]Department of Industrial Engineering – DII, University of Trento, Italy

[b]Department of Mechanical and Industrial Engineering, NTNU – Norwegian University of Science and Technology, Trondheim, Norway

[c]Department of Civil and Industrial Engineering – DICI, University of Pisa, Italy

*Corresponding author

Matteo Benedetti

Email: matteo.benedetti@unitn.it

Tel: +390461282457

Abstract

A novel strain-energy-density (SED) based fatigue criterion is here proposed to account for the effect of mean stress and plasticity on the uniaxial fatigue strength of plain and notched components. It is based on the definition of four SED components: $\Delta\overline{W}_{el}$, the elastic SED associated to the stress range, $\Delta\overline{W}_{el,\max}$, the maximum elastic SED in the stabilized cycle, $\Delta\overline{W}_{pl}$, the plastic SED dissipated per stabilized cycle, $\overline{W}_{pl,\max}$, the plastic SED dissipated over the cycles until stabilization. The mean stress effect is incorporated in a Walker-like expression, $\Delta\overline{W}_{el}^{a}\overline{W}_{el,\max}^{1-a}$, while $\overline{W}_{pl,\max}$ is added to the expression of the total SED to include the effect of mean stress relaxation. An energetic approach is proposed to identify the condition of cycle stabilization. The coefficients of the fatigue criterion are calibrated using experimental fatigue data. The criterion is validated by predictions of independent data.

Keywords

Strain energy density; notch fatigue; mean stress sensitivity; mean stress relaxation; plasticity

Nomenclature

DCI ductile cast iron

FE finite element (method)

HCF	high-cycle fatigue
QT	quenched and tempered
SED	strain energy density
c_W	mean stress sensitivity factor according to Eq. (1c)
E	Young's modulus
N	number of cycles
N_f	number of cycles to failure
N_{st}	number of cycles at stabilization
R	load ratio
R	notch root radius
r_0	circular control area centre position
R_1	control radius
W	strain energy density
$\overline{W}$	strain energy density averaged over the domain Ω shown in Fig. 1a
α	mean stress sensitivity factor
$\bar{a}$	V-notch opening half-angle
β	factor accounting for plastic work dissipated until stabilization
C, γ	coefficients of Chaboche plastic material model
δ	factor accounting for plastic work dissipated per cycle at stabilization
δW	strain energy density range
Δσ	stress range
ΔW	strain energy density associated to the stress range
$D\overline{W}_1$	material dependent fatigue strength characteristic
$D\overline{W}_{ref}$	reference strain energy density used to define the convergence parameter κ (Eq. (4a))
κ	convergence parameter (Eq. (4b))
κ_{st}	threshold of the convergence parameter at stabilization
σ	normal stress
σ_0	cyclic yield strength
σ_{YS}	monotonic yield strength
σ_N	notched specimen (net) nominal stress
χ	backstress tensor
ε	normal strain

Subscripts

a amplitude

el elastic

eq equivalent

max maximum

min minimum

pl plastic

1. Introduction

Fatigue assessment in the presence of intricate geometries and complex loading is still an issue, which is nowadays more critical for the advancement of new subtractive and additive techniques which allow unprecedent geometrical complexities and then are subjected to unprecedent degrees of multiaxiality [1].

The concept of strain energy density (SED) has been employed to assess the fatigue behavior of notched components both under uniaxial [2][3] and multi-axial stresses [4][5]. Herein, the stress at the notch tip has been thought as the parameter governing the fatigue behavior of the overall structures. An energy-based criterion for assessing the high cycle multiaxial fatigue life has been proposed in Ref. [6]. The criterion states that the crack initiation occurs as soon as the distortion strain energy exceeds a critical value. A precise link present between energetic and mesoscopic approaches has been found in [7]. This has allowed to explore the fatigue of metals from the scale of the metal grains.

It is obvious that any SED approach strictly speaking cannot be used at the tip of a sharp V-shaped notch since not only the stresses tend toward infinite but also the strain energy density. On the contrary, in a small but finite volume of material close to the notch, whichever its local shape (blunt notch, severe notch, re-entrant corner, crack), the energy always has a finite value and the main question is rather that of estimating the size of this volume. A “critical volume approach” has been employed in high cycle fatigue regime [8] and in low cycle fatigue [9]. A “stress field intensity approach”, in which the product of the equivalent stress and a weight function, has been integrated in a domain whose size is the material-dependent [10][11]. A large amount of results reported for multi-axial fatigue confirmed that the notch geometry may play a significant role in influencing the cracking behavior and that any fatigue life or strength prediction method that only considers surface stress-strain behavior may not be adequate for many notches of practical interest [12]. By taking into consideration a volume of material and not simply a point at the notch tip, may be the simpler choice as proposed in [13]. It has been suggested to use the mean value of the local energy to predict the

static and fatigue behavior of components weakened by sharp V-notches with a strongly variable notch angle $2\bar{\alpha}$. The control radius R_c of the volume, over which the energy was averaged, depends on the ultimate tensile strength and the fracture toughness K_{IC} in the case of static loads and brittle materials. It depends on plain specimen fatigue limit and on the threshold behavior ΔK_{th} in the case of metallic materials under high-cycle fatigue (HCF) loads. The size of the averaging domain Ω for a notch under mode I type of loading will be here denoted as R_1, as schematically indicated in Fig. 1a. A main issue of the approach is how to properly consider the effect of the mean stress that is known to greatly affect the fatigue response of metallic materials. A second relevant problem is how to include into the fatigue calculation the effect of plastic deformation, which is responsible for mean stress relaxation and ratchetting as well as dissipation of strain energy. These two aspects are the focus of the present work. For the sake of simplicity, the present paper will address uniaxial fatigue only, nonetheless it might pave the way for future extensions to multiaxial loading.

It is well established in the scientific and technical literature that the mean stress, and therefore the stress ratio $R=\sigma_{min}/\sigma_{max}$, exerts a marked influence on the fatigue strength of metallic materials [14]. There are different approaches to incorporate the mean stress effect into a strain energy-based fatigue criterion. The first issue that must be addressed is the definition of the variation of SED produced by the cyclic fluctuation of the stress-strain field. To this regard, Lazzarin et al. [15], Lin et al. [16] and Dallmeier et al. [17] suggested considering the variation between maximum and minimum SED occurring during the load cycle. In the simple case of uniaxial stress, this definition is graphically represented by the gray area indicated in Fig. 1b ($0 \le R \le 1$) and 1c ($R < 0$) and expressed by the following equation:

$$\Delta W = \begin{cases} \dfrac{1}{2E}\left(\sigma_{max}^2 - \sigma_{min}^2\right) & 0 \le R \le 1 \\ \dfrac{1}{2E}\left(\sigma_{max}^2 + \sigma_{min}^2\right) & R < 0 \end{cases} \tag{1a}$$

On the other hand, Koh [18] obtained a considerable improvement in the fatigue predictions by considering the SED associated to the stress range $\Delta\sigma = \sigma_{max} - \sigma_{min}$. In the case of uniaxial stress, irrespectively of the stress ratio R, the SED is graphically represented by the dashed area in Fig. 1b and c and takes the following mathematical expression:

$$\Delta W = \frac{1}{2E}\left(\sigma_{max} - \sigma_{min}\right)^2 = \frac{\Delta\sigma^2}{2E} \tag{1b}$$

Lazzarin et al. [15] proposed to reformulate Eq. (1a) so as to make explicit the dependency of ΔW upon the stress range $\Delta\sigma$:

$$\Delta W = c_W \frac{\Delta\sigma^2}{2E}$$

$$c_W = \begin{cases} \dfrac{1-R^2}{(1-R)^2} & 0 \le R \le 1 \\ \dfrac{1+R^2}{(1-R)^2} & R < 0 \end{cases} \tag{1c}$$

The correction coefficient c_W was then used in later works [19][20][21] to account for the mean-stress effect in the fatigue calculations based on the average SED calculated for the reference case R=0 (whereby $c_W = 1$).

In contrast to this last approach, Ellyin and Kujawski [22], Lin et al. [16] and Dallmeier et al. [17] suggested considering only the positive SED on the base of experimental evidences that negative compressive stresses are much less effective than positive tensile stresses in promoting fatigue damage. In the case of uniaxial stress, this criterion is depicted in Fig. 1d for negative stress ratios and takes the following mathematical expression:

$$\Delta W^+ = \begin{cases} \dfrac{1}{2E}\left(\sigma_{max}^2 - \sigma_{min}^2\right) & 0 \le R \le 1 \\ \dfrac{\sigma_{max}^2}{2E} & R < 0 \end{cases} \tag{1d}$$

Very recently, Roostaei et al. [23] proposed an alternative expression for ΔW^+ as a function of the maximum, mean and amplitude of the normal stress.

The assumption of linear-elastic stress field considered so far is reasonable only in the HCF regime of structural metals with low fatigue-strength-to-yield-stress ratio. Ductile metals, especially in the low-to-medium cycle fatigue regime and in the presence of stress raisers, undergo plastic deformation. In general, the stress-strain state undergoes during the first loading cycles mean stress relaxation and ratchetting phenomena [24] [25] until stabilization of the hysteresis loop after a certain number of cycles. As schematically shown in Fig. 1e, the strain energy is partly accumulated and released during the cyclic loading in the form of elastic strain energy and partly dissipated in the form of plastic strain energy. Morrow [26] first observed that the dissipation of plastic work is the main cause of irreversible damage and fatigue failure of materials. Ellyin and Golos [27][28] first proposed the idea of a SED-based fatigue criterion that encapsulates both types of energy contribution according to the following expression:

$$\Delta W_{tot} = \Delta W_{el}^+ + \Delta W_{pl} \tag{1e}$$

Where ΔW_{el}^{+} is the positive elastic SED defined by Eq. (1d) and ΔW_{pl} is the plastic SED, graphically represented in Fig. 1e as the area comprised within the stabilized hysteresis loop. In the expression of the total SED, Ellyin and Golos [27][28] postulated equal contribution of elastic and plastic part to the fatigue damage. Dallmeier et al. [17] observed however that Eq. (1e) tends to overestimate the contribution of the elastic term and thus introduced a weighting coefficient to modulate its relative importance with respect to the plastic term.

Ellyin [29] further extended his elastic-plastic criterion to multiaxial loading by introducing an appropriate multiaxial constraint factor $\bar{r}$ to correct the contribute of the plastic SED ($\bar{r}=1$ for uniaxial loading). Ince and Glinka [30], Liu [31], Liao and Zhu [32] extended the concept of virtual strain energy to elastic-plastic loading conditions. Recently, Zhu et al. [33] proposed a fatigue-creep damage parameter based on the concept that the component is in critical conditions when the plastic SED accumulated until failure equates the material toughness estimated as the product of ductility and strength. Furthermore, Zhu et al. [34] proposed a modified definition of the total SED incapsulating two mean stress correction factors.

Even though providing satisfactory fatigue predictions in a wide variety of situations, this conceptual framework of the SED still leaves room for open questions, which stimulated the present work to attempt further improvements:

1) The effect of mean stresses on the fatigue strength of a metallic material depends on its peculiar mean-stress sensitivity [35], which cannot be properly taken into account only on the base of energetic considerations, as also emphasized by Zhu et al [34].
2) As above discussed, there is no unanimous consensus as to the relative importance of elastic and plastic strain energy density in dictating the fatigue damage. Moreover, investigations done so far focused their attention only on the stabilized hysteresis loop, completely neglecting the stress-strain history prior to stabilization.
3) The size R_1 of the SED averaging domain Ω is often regarded to as a material characteristic inferred from linear elastic analyses in the HCF regime [36], but it is still debated if and to which extent the plastic deformation affects R_1 and its dependency upon the number of cycles to failure N_f, especially in the low-to-medium cycle fatigue regime [37].

To address the aforementioned issues, the present article is aimed at devising a SED-based fatigue criterion able to incorporate the material-dependent mean stress sensitivity and the cyclic evolution of the stress-strain state occurring in smooth and notched parts subjected to uniaxial loading. This fatigue criterion is an evolution of the SED method proposed by Lazzarin and Zambardi [13] and then further developed by Berto and coworkers [38], based on the Beltrami's definition of total SED averaged on a circular domain centered at distance r_0 from the notch tip, as schematically illustrated

in Fig. 1a. The fatigue criterion must be calibrated on the basis of a certain set of material fatigue data and will be validated through the prediction of an independent set of fatigue experiments. For this purpose, a comprehensive set of fatigue data collected by the authors in [39] on two structural metallic alloys, namely 7075-T6 aluminum and 42CrMo4+QT (quenched and tempered) steel, will be used. More specifically, the fatigue experimentation carried out on these two materials also employed notched samples, whose optimal geometry was devised for a robust inverse determination of the SED control radius [37] and the critical length according to the Theory of Critical Distances [40]. The fatigue criterion is further validated by fatigue data carried out in [41] on a Ductile Cast Iron (DCI) under a broad spectrum of load ratios R, ranging from –7 to 0.5. In this way, it is possible to verify the validity of the fatigue criterion also under very large compressive stresses, which are not commonly explored in the scientific literature.

The paper is organized as follows. Section 2 provides the theoretical background of the proposed fatigue criterion. Section 3 illustrates the fatigue data used to calibrate and validate the fatigue criterion. Section 4 describes the method adopted to get an accurate calibration of the Chaboche model of the material's cyclic behavior to be incorporated into the finite element model used in Section 5 to estimate the plastic and elastic SED in the investigated fatigue experiments. The application of the fatigue criterion is discussed in Section 6. Section 7 summarizes the main conclusions of the paper.

2. Definition of the fatigue criterion

Among the mean stress models proposed in the technical literature [14], the Smith-Watson-Topper (SWT) approach [42] was the first to recognize the important role of the maximum stress in dictating the fatigue strength and proved to give acceptable and consistent results for a wide range of materials [35]. Similarly, Walker [43] first argued that the mean stress effect on the fatigue crack growth rate can be accounted for by expressing the crack propagation driving force not only in terms of the range of the stress intensity factor but also of its maximum value. He proposed to use a material-dependent exponent α and its complement to 1, viz. 1-α, in order to modulate the relative importance of range and maximum value, respectively.

The same idea was then applied by Dowling et al. [44] who modified the SWT criterion in order to account for the material mean stress sensitivity. In the present paper, we propose to extend the same concept to a SED-based fatigue criterion. In its formulation under linear-elastic conditions, here denoted as "M1", the range and the maximum value of the average SED are incorporated into a Walker-like equation as follows:

$$\Delta\overline{W}_{eq}^{M1} = \Delta\overline{W}^{a}\,\overline{W}_{\max}^{1-a} = \Delta\overline{W}_{1} \tag{2}$$

The two quantities are graphically represented in Fig. 2a by the dashed and gray areas, respectively, in the simple case of uniaxial stress. Importantly, based on the observations of Koh [18], M1 incorporates the SED associated to the stress range and not the SED variation during the load cycle. It should be noted that, in analogy with SWT and Walker equations, Eq. (2) postulates that no fatigue damage will occur if the maximum normal stress is less or equal to zero, therefore it cannot be applied to compression-compression fatigue loading (R > 1). The over-bar sign in Eq. (2) indicates that the SED is averaged over the control volume Ω (see Fig. 1a) in the case of a non-uniform stress distribution occurring in the vicinity of notches. M1 is a tri-parametric fatigue criterion, in which α, $\Delta\overline{W}_1$ and the control radius R_1 are material constants, which are assumed to depend solely on the number of cycles to failure N_f; their value can be deduced from a calibration procedure based on experimental fatigue data as shown in the following. Values of α can conceivably vary from 0 to 1, viz. from full to zero mean stress sensitivity.

Further, we propose M2 as an extension of the fatigue criterion M1 to elastic-plastic conditions according to the following expression:

$$\Delta\overline{W}_{eq}^{M2} = \Delta\overline{W}_{el}^{a}\,\overline{W}_{el,\max}^{1-a} + \Delta\overline{W}_{pl} + b\cdot\overline{W}_{pl,\max} = \Delta\overline{W}_1 \tag{3}$$

The four SED components herein included are graphically represented in Fig. 2b in the case of uniaxial stress. The two elastic SED components, $\Delta\overline{W}_{el}$ and $\overline{W}_{el,\max}$, are encapsulated in the same fashion as in model M1. $\Delta\overline{W}_{pl}$ represent the plastic SED dissipated per load cycle after stabilization of the hysteresis loop. To reduce as much as possible the number of parameter to be calibrated, in agreement with Ellyin's findings, we propose in M2 to simply include $\Delta\overline{W}_{pl}$ without any weighting factor. Finally, in an attempt to incorporate into the fatigue criterion also the stress-strain history prior to stabilization, M2 takes into account also $\overline{W}_{pl,\max}$, viz. the plastic work cumulatively dissipated during the load history from the first cycle until stabilization of the stress-strain state over the averaging domain Ω. Importantly, $\overline{W}_{pl,\max}$ is accumulated not only during the first loading ramp, but over all the subsequent load cycles until stabilization occurring at the fatigue cyles denoted as N_{st}. To uniquely identify N_{st}, we propose to define the following reference SED:

$$\Delta\overline{W}_{ref} = \Delta\overline{W}_{el}^{a}\,\overline{W}_{el,\max}^{1-a} + \Delta\overline{W}_{pl} \tag{4a}$$

and to use it to introduce the parameter κ expressing the relative variation of $\Delta\overline{W}_{ref}$ between consecutive load cycles N and N+1:

$$\kappa = \frac{\Delta\overline{W}_{ref,N+1} - \Delta\overline{W}_{ref,N}}{\Delta\overline{W}_{ref,N}}; \quad N: \text{ cycle index} \tag{4b}$$

$$\kappa = \kappa_{st} \rightarrow N_{st}$$

As explained in the following, the curve κ vs. N is determined through finite element simulations of the load cycle. Since the material hardening behaviour will be modelled enforcing a Chaboche plasticity model based on backstresses evolving exponentially with the accumulated plastic strain, the curve κ vs. N, as schematically shown in Fig. 2c, decays asymptotically, thus full stabilization is never achieved. In this work, we propose an operative definition of the stabilization condition, which is assumed to be achieved when the convergence index κ drops below a threshold value κ_{st}, whose value will be defined in the next sections.

M2 is a four-parameter fatigue criterion, in which the material constants α, $\Delta\overline{W}_1$ and R_1 are assumed to depend solely on the number of cycles to failure N_f. The last parameter b is used to modulate the contribution of $\overline{W}_{pl,\max}$ and, in Section 6, will be assumed to be constant throughout the fatigue life.

Finally, we propose a third criterion, termed M3, in which the contributions of $\Delta\overline{W}_{pl}$ and $\overline{W}_{pl,\max}$ are modulated by two weighting factors that depend on the nominal load ratio R:

$$\Delta\overline{W}_{eq}^{M3} = \Delta\overline{W}_{el}^{a}\,\overline{W}_{el,\max}^{1-a} + d(\mathrm{R})\cdot\Delta\overline{W}_{pl} + b(\mathrm{R})\cdot\overline{W}_{pl,\max} = \Delta\overline{W}_1 \qquad (5)$$

This more general criterion has been introduced to yield satisfactorily accurated predictions in the case of load scenarios with large compressive mean stresses (R<–2). The mathematical expression of δ and β dependency upon R will be introduced in Section 6. We anticipate here that the chosen expressions of δ and β as a function of R make M3 a a nine-parameter fatigue criterion.

In contrast to M1, the application of M2 and M3 criteria is not straighforward, because N_{st} is not known *a priori* and the relation between stresses and SED is not quadratic as in the linear-elastic case. For this purpose, their use necessitates an iterative procedure, whose *modus operandi* is illustrated by the flow chart reported in Fig. 3. In brief, for a given fatigue life N_f and load ratio R, the four SED components of the fatigue criterion are calculated through finite element (FE) simulations of the component of given geometry and subjected to uniaxial loading. After initialization of the iteration index i and definition of the first guess value of the unknown stress amplitude σ_a^0, the terms of Eq. (4) are calculated in order to determine the stabilization cycle N_{st}. Then the equivalent SED is evaluated according to Eq. (3) (M2) or Eq. (5) (M3) and used to get the next estimate of the stress amplitude σ_a^{i+1} by assuming a quadratic relation in a small neighborhood of σ_a^i. This procedure is iterated until convergence. To reduce the number of iterations to convegence, the prediction of the elastic model M1 can be used as a first-guess estimate of the initial stress amplitude σ_a^0; using the experimental data shown in the following, convergence is obtained in this way already after 2 or 3 iterations.

In the next sections, experimental fatigue data will be used to calibrate and validate the above presented fatigue criteria. In particular, a robust determination of the material dependent parameters is performed by least-square fitting a number of experimental fatigue data in excess of the number of parameters. More specifically, the best-fit parameters are obtained through minimization of the following weighted sum of square residuals:

$$WSSE = \sum_{i=1}^{n} \frac{\left(\sigma_{a,i} - \hat{\sigma}_{a,i}\right)^2}{s_i^2} \tag{6}$$

where $\sigma_{a,i}$ is the i-th experimental fatigue strength (amplitude) for a given fatigue life, $\hat{\sigma}_{a,i}$ is its estimator, s_i is its standard deviation, and n is the number of data. Importantly, at least one of these fatigue data must be determined from a notched sample geometry, to catch the dependency upon the control radius R_1, and at least two load ratios must be considered to capture the material mean stress sensitivity. In the following, M1 (tri-parameter), M2 (four-parameter), M3 (nine-parameter) will be calibrated with 4, 6, and 10 fatigue data, respectively.

3. Experimental data

Details regarding the material and experimental procedures used to generate the fatigue data analyzed in this article can be found in [39] regarding 7075-T6 and 42CrMo4+QT and in [41] for 120-90-02 DCI. Their monotonic tensile properties are listed in Table 1.

In [39] the fatigue characterization was carried out under alternating (load ratio R = −1) and pulsating (R = 0.1) axial fatigue on axisymmetric plain and V-notched samples, whose geometry is shown in Figure 4a and c, respectively. V-notch depth and opening angle $2\bar{\alpha}$ (see Fig. 1a) were devised in [40] to maximize the influence of the notch tip singular stress term and hence to minimize the sensitivity of the inverse search of critical distance and control radius to the experimental uncertainties. In [39] notches of different severity were explored by changing the notch root radius R (see Fig. 1a and 4c). In the *sharp* and *blunt* notch configuration, R is set equal to 0.2 mm (effective size measured by SEM is 0.21 mm, theoretical principal stress concentration factor K_t= 5.75) and 1 mm (K_t= 2.88), respectively. Since in [45] it was argued that even at the apex of the sharp notch, the stress field in the 7075-T6 specimens was purely linear-elastic, we investigated in this work a third notched geometry, termed *ultra-sharp*, wherein R is 0.1 mm (effective size 0.12 mm, K_t= 7.42) with the aim of exploring the effect of notch plasticity on the fatigue response of 7075-T6. The SN data along with the fit curves are shown in Figure 5a,b and 5c,d for 7075-T6 and 42CrMo4+QT, respectively.

The experimentation was complemented in [39] by fatigue crack growth tests conducted at R=−1 and R=0.1 using C(T) and M(T) specimens, respectively. The outcomes in terms of crack threshold ΔK_{th} are listed in Table 2. To investigate the cyclic elastic-plastic behavior of 7075-T6 and 42CrMo4+QT,

strain-controlled fatigue tests were performed on axisymmetric hourglass coupons with constant amplitude until final failure. Further details about the experimental procedure are reported in [45]. Stabilized half-life stress-strain hysteresis loops are shown in Fig. 6a and b for 7075-T6 and 42CrMo4+QT, respectively. A certain asymmetry of the hysteresis cycles with respect to the horizontal (strain) axis is evident in both materials, especially at the lowest strain amplitudes. This evidence stimulated in this work the development of an asymmetric Chaboche material model, which will be presented in Section 4.

The fatigue characterization of 120-90-02 DCI was carried out in [41] (a M.Sc. thesis carried out under the supervision of prof. Fatemi, University of Toledo, USA) on axisymmetric plain and V-notched samples (K_t= 3.13), whose geometry is shown in Figure 4b and d, respectively. Axial fatigue tests were carried out using a servohydraulic testing machine under the following load ratios: −7, −3, −1, 0, 1/3, 0.5 (this last one only for plain samples). Fatigue lives until 5×10^6 cycles were explored. The SN displayed a knee around 1×10^6 cycles. The fatigue strength at this fatigue life is selected in this work as a case study application of the proposed fatigue criterion. The fitted SN curves are shown in Fig. 5e and f for plain and notched coupons, respectively. Finally, the material cyclic behavior was characterized through low-cycle stress-controlled fatigue tests, which will be used in Section 4 to determine the parameter of the asymmetric Chaboche material model.

4. Chaboche kinematic hardening model

The Chaboche nonlinear kinematic hardening model [46], with von Mises yield criterion, is considered in this work and the ANSYS software implementation of this model then used. Though more evolved models are available, such as the combined Chaboche isotropic-kinematic hardening [47][48][49][50][51], we did not opt for more complex formulations as they would require additional experimental information for the isotropic hardening component, which is here not available.

The uniaxial formulation of the Chaboche model can be solved in closed form, obtaining a piecewise solution for each positive and negative phases of the loading cycle (or loading and unloading). Multiple and independent backstress components are superimposed to introduce a nonlinearity and provide enough constitutive degrees of freedom. In the present analysis, three components are considered:

$$\alpha = \sum_{1}^{3} \alpha_i \tag{7}$$

Each backstress component α_i evolves according to the differential equation:

$$\mathrm{d}\alpha_i = C_i \,\mathrm{d}\varepsilon_{\mathrm{pl}} - \gamma_i \alpha_i \,\mathrm{d}p \tag{8}$$

where C_i and γ_i are the Chaboche material parameters, $d\varepsilon_{pl}$ is the differential of the plastic strain ε_{pl}, and dp is the accumulated plastic strain increment $dp = |d\varepsilon_{pl}|$. By replacing dp either with $d\varepsilon_{pl}$ or $-d\varepsilon_{pl}$, Eq. (8) can be solved, just distinguishing between the positive and the negative phases [52][53], and, after introducing a sign term m, a unique formula can be derived [25]:

$$\alpha_i = m\frac{C_i}{\gamma_i} + \left(\alpha_{0i} - m\frac{C_i}{\gamma_i}\right)\exp\left(-\gamma_i\left|\varepsilon_{pl} - \varepsilon_{pl0}\right|\right) \tag{9}$$

where $m = 1$ for the positive loading and $m = -1$ instead for the negative loading phase.

The stress σ is finally deduced from the von Mises equation, which, for the uniaxial condition, reduces to:

$$\sigma = m\sigma_0 + \alpha \tag{10}$$

and again $m = 1$ or $m = -1$ for the loading and unloading phases, respectively.

In principle, σ_0 is equivalent to the material yield strength. However, a smaller value can be introduced (compare σ_0 in Table 3 with σ_{YS} reported in Table 1) to properly model the evidence of hysteresis, and then relaxation or ratcheting, even with a stress amplitude smaller than the yield strength [25].

If one of the γ_i parameter is set to zero, such the last one: $\gamma_3 = 0$, as significantly considered later, the form of Eq. (8) gets simpler and its solution reduces to:

$$\alpha_i = \alpha_{0i} + C_i(\varepsilon_{pl} - \varepsilon_{pl0}) \tag{11}$$

This equation is valid both for the positive and the negative loading phases, indeed no absolute value remains in the equation, and its meaning is that the backstress is just linearly related to the plastic strain [54]. An equivalent result could be obviously obtained by introducing a very small γ_i value, however, without a clear evidence of its role in the backstress evolution. The initial conditions for each backstress component α_{0i} and the plastic strain ε_{pl0} are usually set as zero at the beginning of the loading history. And then, in order to preserve the continuity, after any positive or negative loading phase, these terms assume the last value before the load inversion.

The Chaboche model parameters are usually identified with the uniaxial analytical formulation, combined with experimental cyclic tests. The parameter search is generally aimed at accurately simulate the cyclic (stabilized) stress-strain loops. More specifically, the single highest stress amplitude cycle is considered to give a more robust coefficient determination, as suggested by Kumar

and Singh [55]. More elaborate approaches have been proposed in the literature, for example by additionally considering a ratcheting test, provided that this experimental data is available [25] [54]. Very accurate stabilized cyclic reproduction, in fact, does not imply a correct modelling of the ratcheting behavior [53].

In this work, the DCI investigated in [41] is analyzed and the Chaboche kinematic hardening model, with three backstress components, is fitted by considering the highest amplitude stabilized cyclic curve. The fitting points and the Chaboche model loading history are reported in Fig. 7a, and the obtained coefficient values are listed in Table 3. The initial yield stress σ_0 is not imposed, thus it is obtained as a parameter optimization result, such as the other coefficients. The Chaboche model is finally validated with a single element model in ANSYS, by imposing the same constitutive law, as evident in Fig. 7a.

The third component of the Chaboche model is set with $\gamma_3 = 0$, while the other parameters are left not imposed before the optimization. As evident below, and discussed in the literature [47], the term *i*-th with $\gamma = 0$ produces the strain stabilization both in a large stress tensile test and, more significantly, in ratcheting tests. For this reason, the corresponding C coefficient, should be better set by considering a ratcheting test, as proposed by Bertini et al. [25]. In this work, the C_3 coefficient is fixed by considering the ratcheting simulation presented below, after a preliminary fit, then all the remaining material coefficients: $\sigma_0, C_1, \gamma_1, C_2, \gamma_2$ are fitted again on the experimental data.

The 7075-T6 aluminum alloy and the 42CrMo4+QT steel investigated by Santus et al. [39] have been also cyclically tested in the elastic-plastic regime, and again the highest strain amplitude stabilized curves are fitted. These fit results are shown in Figs. 1 (b) and 1 (c), both these metal alloys are tested by imposing a reversed strain amplitude, leading to a not fully alternating stress cycle. The slight asymmetry, encountered for these two materials, is easily simulated by imposing a non-zero initial plastic strain, as evident in the figures. This effect can be considered due to any previous strain experienced by the material during the manufacturing. Nevertheless, a very accurate fit is achieved after calibrating this initial condition and, though the stress asymmetry, the cyclic stabilization is obtained in a quite few load cycles. The obtained Chaboche coefficients are listed in Table 3 for all the three investigated materials.

Figure 8a shows the simulation of a ratcheting test with load ratio $R = -1/7$ and stress amplitude $\sigma_a = 508\,\text{MPa}$, resembling a fatigue test presented below, yet with reversed minimum and maximum stresses. The stabilization of this ratcheting example is obtained in approximately 150 cycles and it is in reasonable agreement with the stabilization sequence reported by Meyer [41]. The stabilization rate strongly depends on the value of C_3. The third backstress follows the C_3 slope, in agreement

with Eq. 11. This steadily increasing term causes the counterslope of the first backstress maxima, while being $C_1/\gamma_1 \ll C_2/\gamma_2$, the second backstress component has a limited role, as shown in Fig. 8b. As a consequence, the nonzero-γ backstress cycles are forced to have null average, and in turn symmetrical cycles are obtained, finally leading to a (plastic) shakedown, as shown in details in Fig. 8c. The stabilized cycles and the backstress components evolutions are reported also for the aluminum alloy and the steel investigated in this paper, as illustrated in Fig. 8 (d)-(e) and Fig. 8 (f)-(g), respectively. Since C_1/γ_1 and C_2/γ_2 are of similar magnitudes, for the aluminium alloy, both these backstress components show a significant counterslopes, and the sum of them equals the C_3 slope. On the contrary, considering 42CrMo4+QT, the role of the backstress component 2 counterslope is simply null, in similarity with DCI. However, the stabilization process is quite faster due to the relatively higher C_3 value in comparison to C_1 and C_2.

5. Finite element modelling of the elastic-plastic stress field

The Chaboche hardening model presented in Section 4 is here used to estimate, by finite element (FE) modelling, the elastic-plastic stress field and the SED in the fatigue experiments conducted on plain, notched and cracked specimens discussed in Section 3.

The FE models are elaborated and solved using the ANSYS 19 commercial code. Specifically, plain and notched samples are analyzed using an axisymmetric model employing quadratic 8-node isoparametric elements (PLANE183). Figure 9a illustrates the mesh in the notch region, which was refined in the same fashion to that used in [37] with the purpose of better reproducing stress and strain gradients at the notch tip. Specifically, the convergence analyses carried out in [37] showed that the chosen level of mesh refinement is able to estimate SED with a relative deviation less than 10^{-4}% from the estimations obtained using the maximum explored level of mesh refinement, which in turn was found to be in very good agreement with SED estimations published in [57] on infinitely sharp notched specimens. The discretization of the critical volume of radius R_1 is obtained by creating a circular area in the FE model centered at distance r_0 from the notch tip. It is thus possible to determine the SED directly from the subset of elements belonging to this area, thus limiting discretization errors as much as possible in the definition of the critical volume contour.

The FE model of the cracked body is depicted in Fig. 9b. It employs plane strain quadratic 8-node elements and is devised to reproduce the configuration of a finite plate with a central through crack under tension. Only one quarter of the body is modelled by enforcing proper symmetry constraints. To limit edge effects, the external dimension W of the body has been selected in order to bring the stress intensity factor relative deviation from that predicted by the Griffith crack model below 1%. In addition, the size of the crack length a and of the uncracked ligament W-a are selected so as to

reproduce the condition of small scale yielding, occurring when the crack tip plastic zone radius r_y is sufficiently small with respect to the region of *K*-dominance, viz. when the following requirement is satisfied [58]:

$$a \geq 2.5\left(\frac{K_I}{\sigma_{YS}}\right)^2 \tag{12}$$

Since the model is used to reproduce also the cracked M(T) specimen configuration adopted for fatigue crack growth experiments under negative load ratio R, the interpenetration between crack faces is prevented by an array of contact elements created on the crack surface and coupled with rigid target elements lying on the crack symmetry plane, as shown in Fig. 9b.

The above described FE models are used to simulate the loading history experienced by the samples during testing. For each loading cycle, the SED is calculated and stored by means of ad-hoc Ansys Parametric Design Language scripts. Specifically, the range (maximum value) of elastic SED is estimated for each element lying in the control volume starting from element results in terms of range (maximum value) of stress and elastic strain components. In addition, the accumulated plastic SED per cycle is computed in each element by internal Ansys routines. These elemental SED components are finally used to compute the corresponding SED components averaged over the control volume.

To provide the reader with a clear picture of the stress-strain response occurring during the investigated fatigue experiments, the axial stress and strain components at the notch apex and in the smooth samples are extracted from the FE results. It is found that, in the HCF regime, the stress distribution is purely elastic in 7075-T6, also in the sharpest notch configuration. As shown in Fig. 10a, a small plastic zone arises at the tip of the sharp and ultra-sharp notch only at stress amplitudes leading to fatigue failure after 10^6 cycles or even fewer.

On the contrary, the stress distribution in 42CrMo4+QT and DCI is elastic-plastic in plain and notched samples even in the HCF regime. This evidence is well depicted in Fig. 10b-d and e-g for 42CrMo4+QT and DCI, respectively; here, the simulations are conducted at stress amplitudes corresponding to the longest fatigue considered in the present work, viz. 10^7 and 10^6 for 42CrMo4+QT and DCI, respectively. When 42CrMo4+QT is tested under fully reversed axial loading (R=−1), there is an immediate stabilization of the elastic-plastic hysteresis loop. Conversely, under R=0.1, the initial loading ramp results in accumulation of plastic deformation, followed by an elastic shakedown in smooth (Fig. 10b) and blunt-notched (Fig. 10c) specimens already during the first unloading ramp. On the contrary, in the sharp-notched specimen (Fig. 10d), mean stress relaxation occurs over some tens of cycles until stabilization.

DCI displays a behavior similar to 42CrMo4+QT when tested under R=−1 (Fig. 10f) and R=0 (Fig. 10g), apart from some evidences of ratchetting occurring in the plain sample at R=0. Fig. 10e refers

to elastic-plastic conditions arising under very large compressive minimum stresses (R=−7), but is representative also of all the conditions characterized by negative compressive mean stresses (R<−1): both plain and notched samples require many loading cycles before stabilization, with a pronounced mean stress relaxation occurring in the notched coupon.

When a notched component experiences a remote load cycle with nonzero mean stress, relaxation occurs with a trend which resembles a controlled strain test, despite of a ratcheting component [56]. The stabilized cycle mean stress depends on the material parameters, and on C_3 in particular, thus the tuning of this coefficient is crucial. Whenever C_3 is relatively low, an almost complete relaxation is obtained. On the contrary, a large value of C_3 results in plastic shakedown with significant nonzero mean stress. As shown in Fig. 10e-g, two trends were observed for DCI: the mean stress either reduces almost to zero when the shakedown is plastic, or just remains unchanged in the case of elastic shakedown. More specifically, the plastic shakedown occurs under compression loading, whereas the elastic shakedown takes place under tensile loading due the smaller stress amplitude. On the contrary, an intermediate mean stress stabilization was observed for 42CrMo4+QT with sharp notch. Finally, for 7075-T6, the stress amplitudes of the pulsating fatigue tests are quite low, thus not inducing any shakedown.

From the above discussion, it is clear that a sound application of criteria M2 (Eq. (3)) and M3 (Eq. (5)) necessitates a clear identification method of the cycle index N_{st} at which stabilization has taken place. The energetic approach expressed by Eq. (4) has the advantage of being representative of the overall situation occurring in the control volume Ω, hence not limited to the notch apex along the axial direction as the plots of Fig. 10. Moreover, these plots indicate an evolution of the stress-cycles in terms of both stress and strain extremes; this makes cumbersome the definition of a convergence criterion based on stresses or strains considered separately. Figure 11a,b,c illustrates the evolution of the convergence parameter κ as a function of the cycle index N in the explored specimen geometries for 7075-T6, 42CrMo4+QT and DCI, respectively. It can be noted that, for material, geometry and loading configurations resulting in an immediate stabilization of the hysteresis loop, κ drops below the limiting value of 5×10^{-4} already after the first cycle. Interestingly, in the case of the plane DCI sample tested under R=−7, this threshold condition is achieved after 180 cycles, in agreement with similar observations reported in Section 4. Consequently, in the remaining part of this article, fatigue predictions will be done considering $\kappa_{st}=5\times10^{-4}$, as also indicated in the flowchart of Fig. 3.

6. Results and discussion

The parameters of the fatigue criteria calibrated in the HCF regime are listed in Table 4. Their application is shown in Figure 12, 13 and 14 and in Tables 5, 6 and 7 for 7075-T6, 42CrMo4+QT and DCI, respectively. The fatigue data indicated in Tables 5, 6 and 7 as "self-consistency tests" were used to calibrate the corresponding fatigue criteria. First, the outcomes of the linear-elastic criterion M1 will be presented and then those of the elastic-plastic criteria M2 and M3.

6.1 Linear-elastic fatigue criterion M1

The tri-parameter fatigue criterion M1 is calibrated for the three investigated materials according to the least-square method expressed by Eq. (6). Specifically, four fatigue data are used, two of them referring to the plain specimen geometry, the remaining two to the sharpest available notch configuration in agreement with the outcomes of our recent work [37], showing that the sensitivity of the control radius inverse search to experimental uncertainties declines with decreasing notch root radius. These fatigue data are obtained under fully-reversed (R=−1) and pulsating (R=0 or R=0.1) axial loading. The best-fit coefficients are listed in Table 4. Interestingly, the mean-stress-sensitivity factor α is about 0.5 for 7075-T6 (a very similar value is indicated in [44] for the Walker coefficient of the same material) and DCI, while for 42CrMo4+QT it takes an unusually high value representative of very low mean stress sensitivity. Table 5a, 6a, and 7a compare the experimental HCF data with the predictions of the fatigue data used for the calibration (self-consistency test) and of the remaining independent fatigue tests (validation test). The stress field is assumed linear-elastic also in the cracked configurations used to estimate ΔK_{th}. It can be noted that the absolute relative error for 7075-T6 (Table 5a) is very low (below 5%) for all the experiments apart from the C(T) specimen tested at R=0.1. In 42CrMo4+QT (Table 6a), the absolute relative error is very low (below 3%) only in the self-consistency tests, while it takes larger values in the validation tests (up to 10%). In particular, the difficulty of linear-elastic fatigue calculation methods in accurately predicting the fatigue strength of the blunt notched specimen at both stress ratios was already found in [37] [39] [45]. The fatigue predictions of DCI (Table 7a) are accurate (absolute relative error below 7%) for load ratios comprised in the range $-1 \le R \le 1$, whereas larger discrepancies (up to 24%) are found for R=−3 and R=−7.

The approach followed so far is then extended to the medium cycle fatigue regime for 7075-T6 and 42CrMo4+QT. For this purpose, the parameters of Eq. (2) are calibrated from the plain and the sharp-notch fatigue data taken at different fatigue lives N_f. Figure 12a and 13a (solid lines) shows the dependency of the criterion parameters a and $\overline{W}_1$ upon N_f. The control radius R_1 is plotted in Fig. 12b and 13b (solid lines) as a function of N_f. Interestingly, the mean stress sensitivity $(1-a)$ and R_1 decline with longer fatigue lives. Figure 12c and 13c (solid lines) shows the predicted SN curves for

the self-consistency tests, Figure 12d and 13d (solid lines) for the validation tests. It can be noted for 7075-T6 that the agreement with the experimental data is very good, apart from the predictions of the samples tested under R=0.1 at short fatigue lives ($N_f \leq 5 \cdot 10^5$). While the self-consistency tests for 42CrMo4+QT are in very good agreement with the experimental data, there is a significant underestimation and overestimation of the blunt specimens tested under R=−1 and R=0.1, respectively (see Fig. 13d).

From the analysis of the elastic-plastic stress field discussed in Section 5, it is clear that the aforementioned discrepancies should be mainly ascribed to the deviation of the actual stress-strain field from the assumption of linear-elastic material response. If we want to further improve the already satisfactory predictions of the proposed fatigue criterion, we need to consider the actual elastic-plastic stress distribution.

6.2 Elastic-plastic fatigue criteria M2 and M3

The four-parameter fatigue criterion M2 is calibrated for 7075-T6 and 42CrMo4+QT according to the least-square method expressed by Eq. (6). Specifically, six fatigue data are used, four of them are the same as in Section 6.1, the remaining two are the crack growth thresholds determined at R=−1 and R=0.1. The approach followed for the calibration is different in the two materials: since the plain and notched fatigue data of 7075-T6 are in linear elastic regime, the three parameters in common with M1, viz. a, $\overline{W}_1$ and R_1, are kept the same as in M1. Therefore, the crack thresholds data are used exclusively to calibrate the plastic parameter β. Conversely, in 42CrMo4+QT, all six fatigue data are refer to elastic-plastic conditions, therefore they are fully recalibrated. The best-fit parameters are listed in Table 4. Interestingly, the exponent a takes now for 42CrMo4+QT a more usual value of about 0.4, the control radius R_1 reduces by more than one half with respect to M1. For both materials, even though greatly differing in absolute value, the plastic parameter β takes a negative value. This outcome is very interesting, as it indicates that the relaxation of tensile mean stresses occurring for $-1 \leq R \leq 1$ in the first cycles until stabilization is beneficial to the fatigue response and therefore the accumulated plastic work $W_{pl,\max}$, thanks to the negative sign of β, contributes to reduce the equivalent SED $\Delta\overline{W}_{eq}^{M2}$. The HCF predictions listed in Table 5b and 6b indicate a further accuracy improvement, especially for 42CrMo4+QT, where the RMS relative error declines from 6.1% to 1.7%, mainly thanks to the more accurate fatigue calculation of the blunt specimens (validation test). The extension of M2 criterion to the medium cycle fatigue regime is not straightforward, as its robust calibration necessitates a number of fatigue tests in excess with respect to those available in this fatigue regime, wherein a fracture mechanics parameter representative of the crack growth resistance

is not clearly defined. In a first attempt to overcome this limitation, we decided to extend the value of β, calibrated in the HCF regime, to the entire fatigue life interval. The elastic-plastic calibration is thus limited to the parameters a, $\overline{W}_1$ and R_1. As expected, for 7075-T6 (Fig. 12a and b, dashed lines), the M2 parameters significantly differ from the M1 ones only at fatigue lives shorter than 5×10^5, while for 42CrMo4+QT (Fig. 13a and b, dashed lines), the difference is remarkable throughout the fatigue life. As shown in Fig. 12c and d (dashed lines), there is a slight improvement in the prediction of the fatigue strength of 7075-T6 samples tested under R=0.1. The self-consistency tests in 42CrMo4+QT (Fig. 13c, dashed lines) lead to predictions very similar to M1, apart from the plain samples tested under R=−1, whereas the validation tests of the blunt notched variants (Fig. 13d, dashed lines) are in significantly better agreement with the experimental data.

The calibration of the elastic-plastic fatigue criterion is performed for DCI in a different way, mainly for two reasons. First, no crack threshold data are available for this material. Therefore, the calibration must be based on plain and notched specimen geometries, only. When calibrating M2 with fatigue data referring to plain and notched specimens tested at R=−1, 0, 1/3 (positive or null mean stress), the best-fit value of the plastic parameter β is −0.105. This value is close to that found for 42CrMo+QT and its negative sign is coherent with the above observation that the relaxation of tensile mean stresses is beneficial to the fatigue strength. However, when the so calibrated criterion M2 is used for fatigue calculation at $R < -1$, it results in inconsistent predictions. From one side, this is not surprising, because we expect that the relaxation of compressive mean stresses is detrimental to the fatigue behavior, implying a change in the sign of β in this fatigue regime. On the other hand, unexpectedly, we found that not only β but also the weighting factor of $\Delta\overline{W}_{pl}$ must change for $R < -1$. This stimulated the definition of the criterion M3 able to extend M2 to load scenarios with negative mean stresses. Specifically, we introduce a further weighting factor δ, which along with β is assumed to be a function of the load ratio R. In particular, a sigmoidal variation of proposed according to the following hyperbolic functions:

$$\begin{aligned} \delta(R) &= \mathrm{Tanh}(d_1 \times R + d_2) \\ \beta(R) &= b_1 \times \mathrm{Tanh}(b_2 \times R + b_3) + b_4 \end{aligned} \tag{13}$$

Importantly, the function $\delta(R) = \mathrm{Tanh}(d_1 \times R + d_2)$ is intentionally limited to the range $-1 \le \delta(R) \le 1$, as we found that just a sign change in $\Delta\overline{W}_{pl}$ is necessary to achieve satisfactory predictions in the regime $R < -1$. To calibrate the nine-parameter fatigue criterion M3, the plain and notched fatigue data at R = −7, −3, −1, 0, 1/3 are used. The best-fit coefficients are listed in Table 4. The variation of β and δ as a function of R is plotted in Fig. 14b. Interestingly, the sign change of β occurs across of the zero mean stress condition ($R = -1$), while that of δ takes place approximately around $R = -2$.

The outcomes of the fatigue criterion M3 are listed in Table 7b and compared in graphical form with those of the elastic criterion M1 in Fig. 14a. It can be noted that M3 yields predictions very similar to M1 for zero-positive mean stresses ($-1 \le R \le 1$), while the improvement obtained by incorporating the plastic SED components is significant in the compressive mean stress regime ($R < -1$). Accordingly, the maximum absolute error declines from 24% to 7%. Figure 14a reports also the predictions based on the c_W approach (Eq. (1c)), adopted to correct the plain and notched fatigue strength at R=0 for different load ratios. This method works well in the regime $-1 \le R \le 1$, while the discrepancies from the experimental data is significant in the compressive mean stress regime.

To conclude, the negative constant value of β and the unitary value of δ found in DCI in the positive mean stress regime yields a further validation of the M2 criterion successfully applied to 7075-T6 and 42CrMo4+QT in the same R interval. Additional scientific scrutiny is necessary to further support the evidence found in this paper that the plastic work $\Delta\overline{W}_{pl}$ dissipated per cycles is beneficial to the fatigue response at very negative R values. Perhaps, this should be imputed to the assumption taken in the present paper that the remaining criterion parameters, viz. a, $\overline{W}_1$ and R_1, are independent of R.

Desirably, the proposed method will be extended in the future to multi-axial loading conditions. Some points of special attention can be here anticipated: (i) the size of the SED control radius depends on the loading mode [20][21], therefore we expect that the extended formulation of M1, M2, M3 criteria must include this issue; (ii) since the reference SED $\Delta\overline{W}_{ref}$ used to identify the stabilization condition must be averaged over domains of mode-dependent size, we expect an analogous dependency of the number of cycles at stabilization N_{st}; (iii) more sophisticated hardening rules must be adopted to capture the complex evolution of the yield surface under mixed-mode conditions, especially in the presence of out-of-phase loading.

7. Conclusions

A novel SED based fatigue criterion has been proposed to account for the effect of mean stress and plasticity on the uniaxial fatigue strength of plain and notched components. This criterion is based on the definition of four SED components: $\Delta\overline{W}_{el}$, the elastic SED associated to the stress range, $\Delta\overline{W}_{el,\max}$, the maximum elastic SED in the stabilized cycle, $\Delta\overline{W}_{pl}$, the plastic SED dissipated per stabilized cycle, $\overline{W}_{pl,\max}$, the plastic SED cumulatively dissipated over the cycles until stabilization. The mean stress effect is incorporated in a Walker-like expression, $\Delta\overline{W}_{el}^{a}\overline{W}_{el,\max}^{1-a}$, while $\overline{W}_{pl,\max}$ is added to the expression of the total SED to include the effect of the mean stress relaxation. An energy-based approach has been proposed to identify the condition of cyclic stabilization. The cyclic plastic

behavior has been modelled according to the kinematic hardening rule proposed by Chaboche, wherein one of the g_i parameter is set to zero to a achieve strain stabilisation in ratcheting and relaxation loading conditions. The proposed fatigue criteria have been calibrated and validated using experimental fatigue data collected on 7075-T6, 42CrMo4+QT, and 120-90-02 DCI. The following conclusions can be drawn from the present investigation:

1) In the HCF regime, the stress field remains linear elastic for 7075-T6, even at very sharp notches. Conversely, in 42CrMo4+QT and 120-90-02 DCI the stress cycling turns into an elastic-plastic regime, even in plain and blunt-notched specimens.
2) A purely linear-elastic formulation of the proposed fatigue criterion (M1) yields very accurate predictions in the medium-to-high cycle fatigue regime of 7075-T6. When applied to 42CrMo4+QT and 120-90-02 DCI, the fatigue tests used for model calibration are represented with high accuracy, whereas the error in the prediction of validating tests is larger, viz. 10% for 42CrMo4+QT (blunt-notched specimens), and 24% for 120-90-02 DCI (tests under very large compressive minimum stresses). The elastic-plastic formulations of the criterion (M2 and M3) yields a much better assessment of validation tests, as it is capable of encapsulating the effect of plastic SED dissipation and mean stress relaxation. This last aspect represents a specific point of novelty of the present paper, as, to the best knowledge of the authors, none of the SED-based fatigue criteria proposed so far addressed the issue of the load history prior stabilization.
3) The effect of the mean stress relaxation produced by the elastic-plastic redistribution of the stress field is effectively taken into account in M2 and M3 by the SED component $\overline{W}_{pl,\max}$ weighted by a factor β. Its effect changes across the zero mean stress condition, more specifically is beneficial for $-1 \le R \le 1$ and detrimental for $R < -1$.
4) The SED term $\Delta\overline{W}_{pl}$ can be directly incorporated into the expression of the total SED in the range $-2 \le R \le 1$ without any weighting factor δ. Its role under very large compressive minimum stresses ($R < -2$) seems to be beneficial to the fatigue strength and deserves further scientific investigation. Apart from that, an elasto-plastic model (M2) assuming β constant and δ=1 is suitable for elastic-plastic fatigue calculations in the commonly encountered range $-1 \le R \le 1$.
5) While the proposed models yield satisfactorily accurate estimations under uniaxial fatigue, their further validation and modification need to be further investigated under more complex multiaxial loading conditions.

References

[1] Benedetti M, Santus C. Notch fatigue and crack growth resistance of Ti-6Al-4V ELI additively manufactured via selective laser melting: a critical distance approach to defect sensitivity. Int J Fatigue 2019;121:281–92.

[2] Molsky K., Glinka G. A method of elastic-plastic stress and strain calculation at a notch root. Material Science and Engineering 1981;50:93-100.

[3] Glinka G. Energy density approach to calculation of inelastic strain-stress near notches and cracks. Eng. Fract. Mech. 1985;22:485-508.

[4] Moftakhar A., Buczynski A., Glinka G. Calculation of elasto-plastic strains and stresses in notches under multiaxial loading. Int J Fracture 1995;70:357-373.

[5] Park J., Nelson D. Evaluation of an energy-based approach and a critical plane approach for predicting constant amplitude multiaxial fatigue life. Int J Fatigue 2000;22:23-39.

[6] Froustey C., Lasserre S., Dubar L. Validité des critères de fatigue multiaxialee à l'endurance en flexion-torsion (1992) Procs. Mat-Tech '92. IITT-International, France, 79-85 (in French).

[7] Morel F., Palin-Luc T., Froustey C. Comparative study and link between mesoscopic and energetic approaches in high cycle multiaxial fatigue. Int J Fatigue 2001;23:317-327.

[8] Pluvinage G. Rupture and fatigue initiated from notches. Application of the notch intensity factor. Revue Francaise de Mecanique 1997;1:53-61 (in French).

[9] Bentachfine S., Pluvinage G., Gilgert J., Azari Z., Bouami D. Notch effect in low cycle fatigue. Int J Fatigue 1999;21:421-430.

[10] Yao W. Stress field intensity approach for predicting fatigue life. Int J Fatigue 1993;15:234-245.

[11] Yao W., Xia K., Gu Y. On the fatigue notch factor, Kf. Int J Fatigue 1995;17:245-251.

[12] Tipton S.M., Nelson D.V. Advances in multiaxial fatigue life prediction for components with stress concentrations. Int J Fatigue 1997;19:503-515.

[13] Lazzarin P, Zambardi R. A finite-volume-energy based approach to predict the static and fatigue behavior of components with sharp V-shaped notches. Int J Fracture 2001;112(3):275–98.

[14] Sendeckyj G.P. Constant life diagrams — a historical review. Int J Fatigue 2001;23:347-353.

[15] Lazzarin P., Sonsino C., Zambardi R. A notch stress intensity approach to assess the multiaxial fatigue strength of welded tube-to-flange joints subjected to combined loadings. Fatigue Fract Eng Mater Struct 2004;27(2):127-140.

[16] Lin YC, Chen XM, Liu ZH, Chen J. Investigation of uniaxial low-cycle fatigue failure behavior of hot-rolled AZ91 magnesium alloy. Int J Fatigue 2013;48:122–32.

[17] Dallmeier J, Denk J, Huber O, Saage H, Eigenfeld K. Deformation behavior and fatigue analysis of magnesium wrought alloys under variable amplitude loading. Mater Today Proc 2015;2:S119–24.

[18] Koh SK. Fatigue damage evaluation of a high pressure tube steel using cyclic strain energy density. Int J Press Vessel Pip 2002;79:791–8.

[19] Lazzarin P., Livieri P., Berto F., Zappalorto M. Local strain energy density and fatigue strength of welded joints under uniaxial and multiaxial loading, Eng. Fract. Mech. 2008;75(7):1875-1889.

[20] Berto F., Lazzarin P., Yates J. Multiaxial fatigue of V-notched steel specimens: a non-conventional application of the local energy method. Fatigue Fract Eng Mater Struct 2011;34(11):921-943.

[21] Berto F., Campagnolo A., Lazzarin P. Fatigue strength of severely notched specimens made of Ti–6Al–4V under multiaxial loading. Fatigue Fract Eng Mater Struct 2015;38(5):503-517.

[22] Ellyin F, Kujawski D. A multiaxial fatigue criterion including mean-stress effect. Adv Multiaxial Fatigue, ASTM STP 1993;1191:55–66.

[23] Roostaei AA, Pahlevanpour A, Behravesh SB, Jahed H. On the definition of elastic strain energy density in fatigue modelling. Int J Fatigue 2019;121:237-242.

[24] Paula SK, Stanford N, Taylor A, Hilditcha T. The effect of low cycle fatigue, ratcheting and mean stress relaxation on stress–strain response and microstructural development in a dual phase steel. Int J Fatigue 2015;80: 341-348.

[25] Bertini L, Le Bone L, Santus C, Chiesi F, Tognarelli L. High Load Ratio Fatigue Strength and Mean Stress Evolution of Quenched and Tempered 42CrMo4 Steel. Journal of Materials Engineering and Performance 2017;26(8):3784-3793.

[26] Morrow J. Cyclic plastic strain energy and fatigue of metals. Intern Frict Damping Cycl Plast ASTM Int 1965:45–87.

[27] Ellyin F, Golos K. Multiaxial fatigue damage criterion. J Eng Mater Technol 1988;110(1):63–8.

[28] Golos K, Ellyin F. Total strain energy density as a fatigue damage parameter. In: Branco CM, Rosa LG, editors. In advances in fatigue science and technology, proceedings of the NATO Advanced Study Institute. Berlin: Kluwer Academic Publishers; 1989. p. 849–58.

[29] Ellyin F. Fatigue Damage, Crack Growth and Life Prediction. London: Chapman & Hall; 1997.

[30] Ince A, Glinka G. A generalized fatigue damage parameter for multiaxial fatigue life prediction under proportional and non-proportional loadings. Int J Fatigue 2014;62(2):34–41.

[31] Liu KC. A method based on virtual strain-energy parameters for multiaxial fatigue life prediction. In: McDowell DL, Ellis R, editors. American Society for Testing and Materials STP 1191, Philadelphia. 1993. p. 67–84.

[32] Liao D, Zhu SP. Energy field intensity approach for notch fatigue analysis. Int J Fatigue 2019;127:190-202.

[33] Zhu SP, Huang HZ, He LP, Liu Y, Wang Z. A generalized energy-based fatigue–creep damage parameter for life prediction of turbine disk alloys. Eng. Fract. Mech. 2012;90:89-100.

[34] Zhu SP, Lei Q, Huang HZ, Yang YJ, Peng W. Mean stress effect correction in strain energy-based fatigue life prediction of metals. Int. J. Damage Mech. 2017;26(8):1219-1241.

[35] Burger R, Lee YL. Assessment of the mean-stress sensitivity factor method in stress-life fatigue predictions. Journal of Testing and Evaluation 2013;41(2):200-206.

[36] Livieri P, Lazzarin P. Fatigue strength of steel and aluminium welded joints based on generalised stress intensity factors and local strain energy values. Int J Fracture 2005;133(3):247-276.

[37] Benedetti M, Santus C, Berto F. Inverse determination of the fatigue Strain Energy Density control radius for conventionally and additively manufactured rounded V-notches. Int J Fatigue 2019;126:306–318.

[38] Berto F, Lazzarin P. Recent developments in brittle and quasi-brittle failure assessment of engineering materials by means of local approaches. Mater Sci Eng R: Reports 2014;75:1–48

[39] Santus C, Taylor D, Benedetti M. Experimental determination and sensitivity analysis of the fatigue critical distance obtained with rounded V-notched specimens. Int J Fatigue 2018;113:113–25.

[40] Santus C, Taylor D, Benedetti M. Determination of the fatigue critical distance according to the Line and the Point Methods with rounded V-notched specimen. Int J Fatigue 2018;106:208–18.

[41] Meyer N. Effects of mean stress and stress concentration on fatigue behavior of ductile iron, M.Sc. thesis, The University of Toledo, Theses and Dissertations, paper 1782 (2014). http://rave.ohiolink.edu/etdc/view?acc_num=toledo1418332368.

[42] Smith RN, Watson P, Topper TH. A stress–strain parameter for the fatigue of metals. J Mater 1970;5(4):767–78.

[43] Walker EK. The effect of stress ratio during crack propagation and fatigue for 2024–T3 and 7075–T6 aluminum. West Conshohocken PA USA: American Society for Testing and Materials; 1970. p. 1–14.

[44] Dowling NE, Calhoun CA, Arcari A. Mean stress effects in stress-life fatigue and the Walker equation. Fatigue Fract Eng Mater Struct 2009;32:163-179.

[45] Benedetti M, Santus C. Mean stress and plasticity effect prediction on notch fatigue and crack growth threshold, combining the theory of critical distances and multiaxial fatigue criteria. Fatigue Fract Eng Mater Struct 2019;42(6):1228–46.

[46] Chaboche JL. Time-independent constitutive theories for cyclic plasticity, Int J Plasticity 1986;2(2):149–188.

[47] Koo GH, Lee JH. Investigation of ratcheting characteristics of modified 9Cr–1Mo steel by using the Chaboche constitutive model. Int J Press Vessel Pip 2007;84(5):284–292.

[48] Broggiato GB, Campana F, Cortese L. The Chaboche nonlinear kinematic hardening model: calibration methodology and validation, Meccanica 2008;43(2):115–124.

[49] Badnava H, Pezeshki SM, Nejad KF, Farhoudi HR. Determination of combined hardening material parameters under strain controlled cyclic loading by using the genetic algorithm method. Journal of Mechanical Science and Technology 2012;26(10):3067–3072.

[50] Koo S, Han J, Marimuthu KP, Lee H. Determination of Chaboche combined hardening parameters with dual backstress for ratcheting evaluation of AISI 52100 bearing steel. Int J Fatigue 2019;122:152–163.

[51] Nath A, Ray KK, Barai SV. Evaluation of ratcheting behaviour in cyclically stable steels through use of a combined kinematic-isotropic hardening rule and a genetic algorithm optimization technique. International Journal of Mechanical Sciences 2019;152:138–150.

[52] Rezaiee-Pajand M, Sinaie S. On the calibration of the Chaboche hardening model and a modified hardening rule for uniaxial ratcheting prediction. International Journal of Solids and Structures 2009;46(16):3009–3017.

[53] Mahmoudi AH, Pezeshki-Najafabadi SM, Badnava H. Parameter determination of Chaboche kinematic hardening model using a multi objective Genetic Algorithm. Computational Materials Science 2011;50(3):1114–1122.

[54] Agius D, Kajtaz M, Kourousis KI, Wallbrink C, Wang CH, Hu W, Silva J. Sensitivity and optimization of the Chaboche plasticity model parameters in strain-life fatigue predictions. Materials & Design 2017;118:107–121.

[55] Kumar P, Singh A. Experimental and Numerical Investigations of Cyclic Plastic Deformation of Al-Mg Alloy. Journal of Materials Engineering and Performance 2019;28(3):1428–1440.

[56] Kourousis KI, Dafalias YF. Constitutive modeling of Aluminum Alloy 7050 cyclic mean stress relaxation and ratcheting. Mechanics Research Communications 2013;53:53–56.

[57] Berto F, Lazzarin P. A review of the volume-based strain energy density approach applied to V-notches and welded structures. Theoret Appl Fract Mech 2009;52(3):183–94.

[58] Anderson TL. Fracture Mechanics: Fundamentals and Applications. Boca Raton (FL): CRC Press; 1995.

Figures

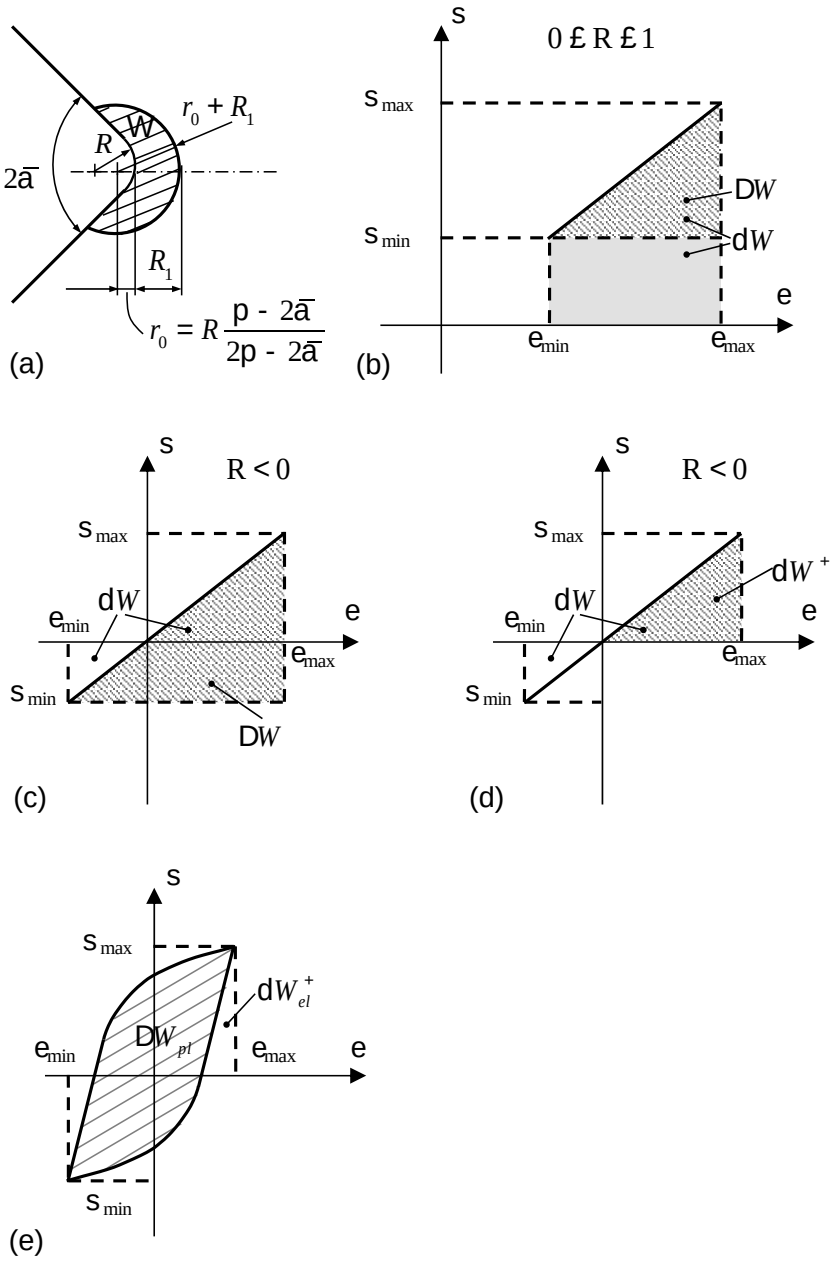

Fig. 1. (a) strain energy density averaging domain Ω ahead of the notch root. (b) and (c) definition of the strain energy density associated to the stress range, in contrast to strain energy density range for positive and negative stress ratio, respectively (d) definition of positive strain energy density (e) Elastic and plastic part of strain energy density.

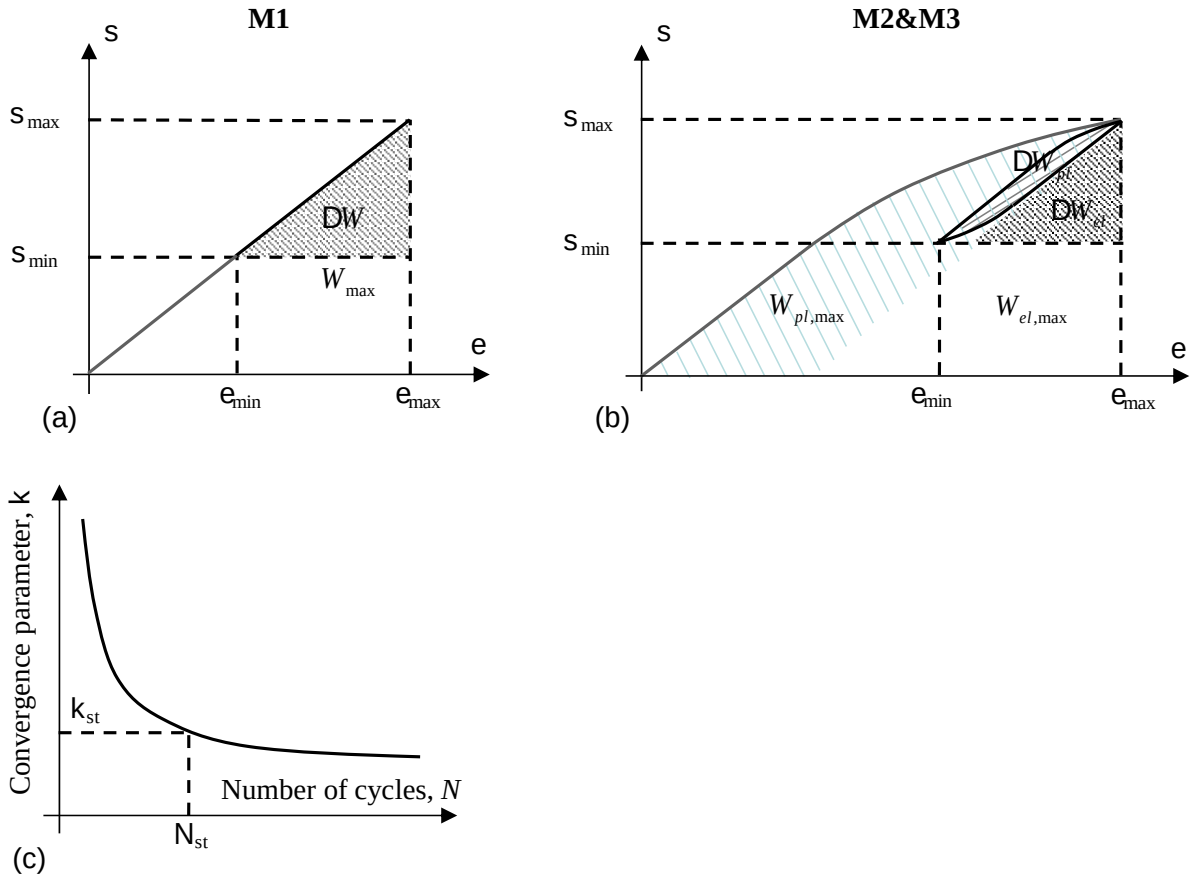

Fig. 2. Definition of strain energy density components considered in the fatigue criterion under (a) linear elastic and (b) elastic plastic conditions. (c) Convergence criterion to estimate the number of cycles N_{st} until stabilization of the elastic-plastic stress-strain field. $\overline{W}_{pl,\max}$ is the plastic strain energy accumulated until stabilization at N_{st}.

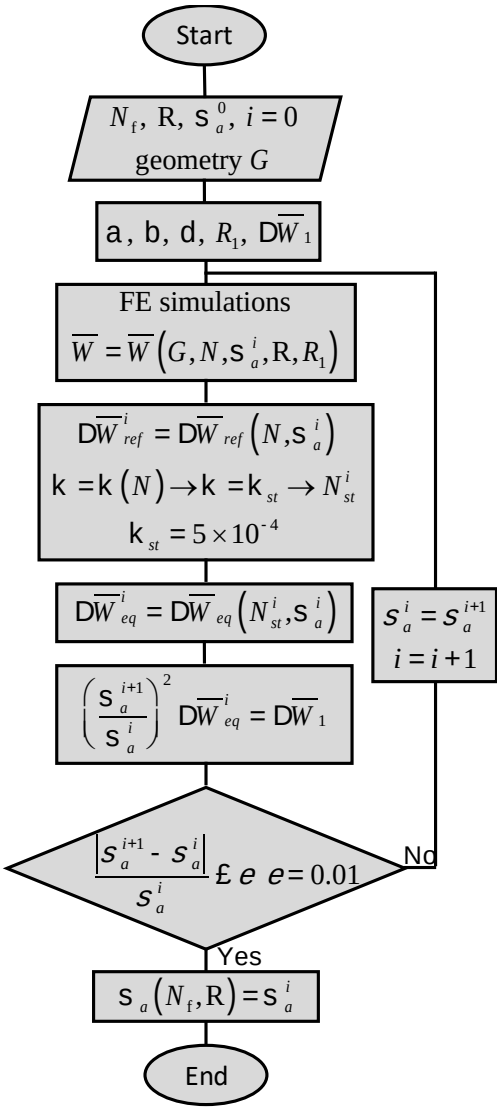

Fig. 3 Flow chart illustrating the application of the elastic-plastic fatigue criteria M2 and M3.

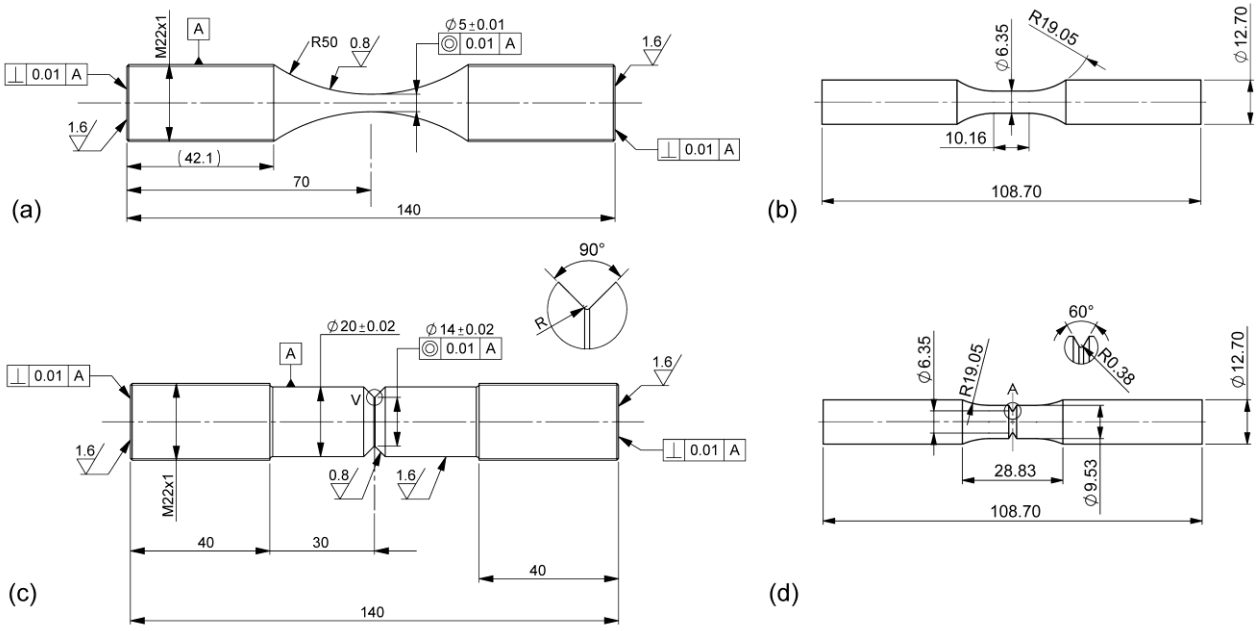

Fig. 4. Geometry of the specimens used to collect the fatigue data elaborated in the present paper. (a) and (b) plain, (c) and (d) notched specimens. (a) and (c) were used for 7075-T6 and 42CrMo4+QT, (d) and (d) for 120-90-02 DCI. In (c) the nominal notch root radius *R* is 1 mm, 0.2 mm and 0.1 mm for blunt, sharp and ultra-sharp notches, respectively.

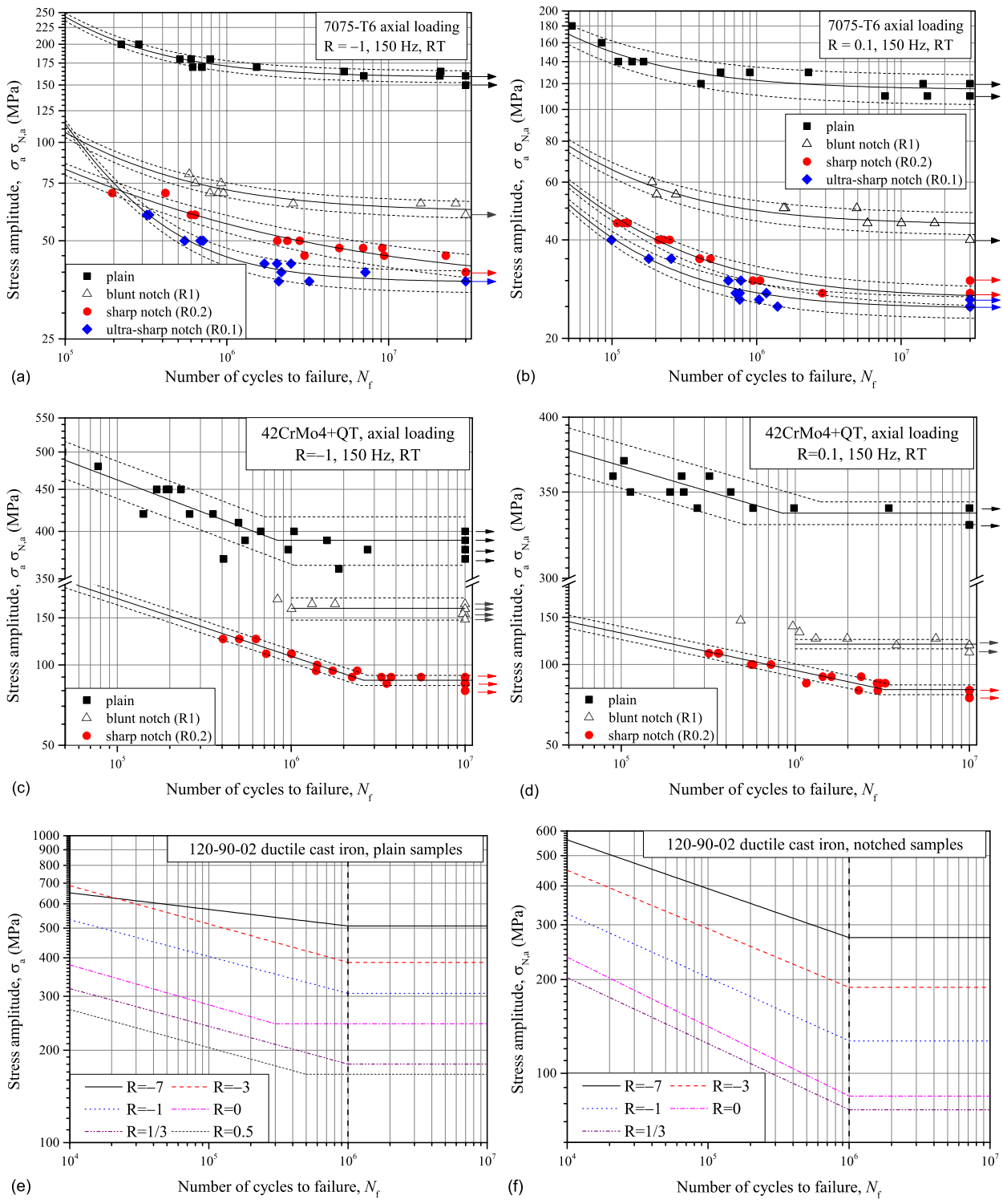

Fig. 5. SN Wöhler curves of the investigated materials. (a) and (b) 7075-T6, (c) and (d) 42CrMo4+QT, (e) and (f) 120-90-02 DCI. (a) and (c) load ratio R = −1, (b) and (d) R = 0.1. (e) plain, (f) notched samples.

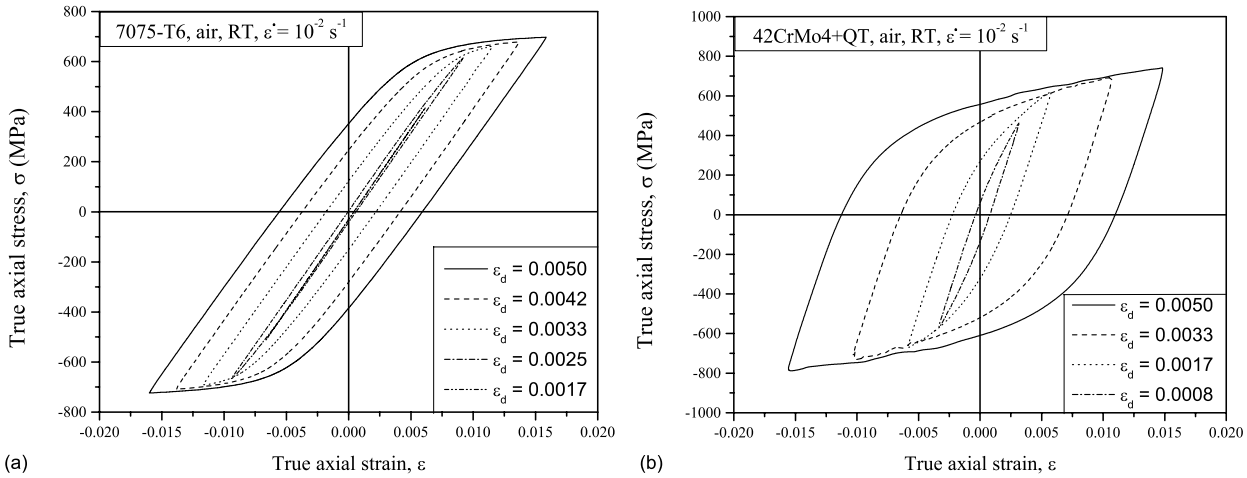

Fig. 6. Stabilized hysteresis loops at half fatigue life. ε_d is the diametrical strain amplitude imposed during the strain-controlled tests.

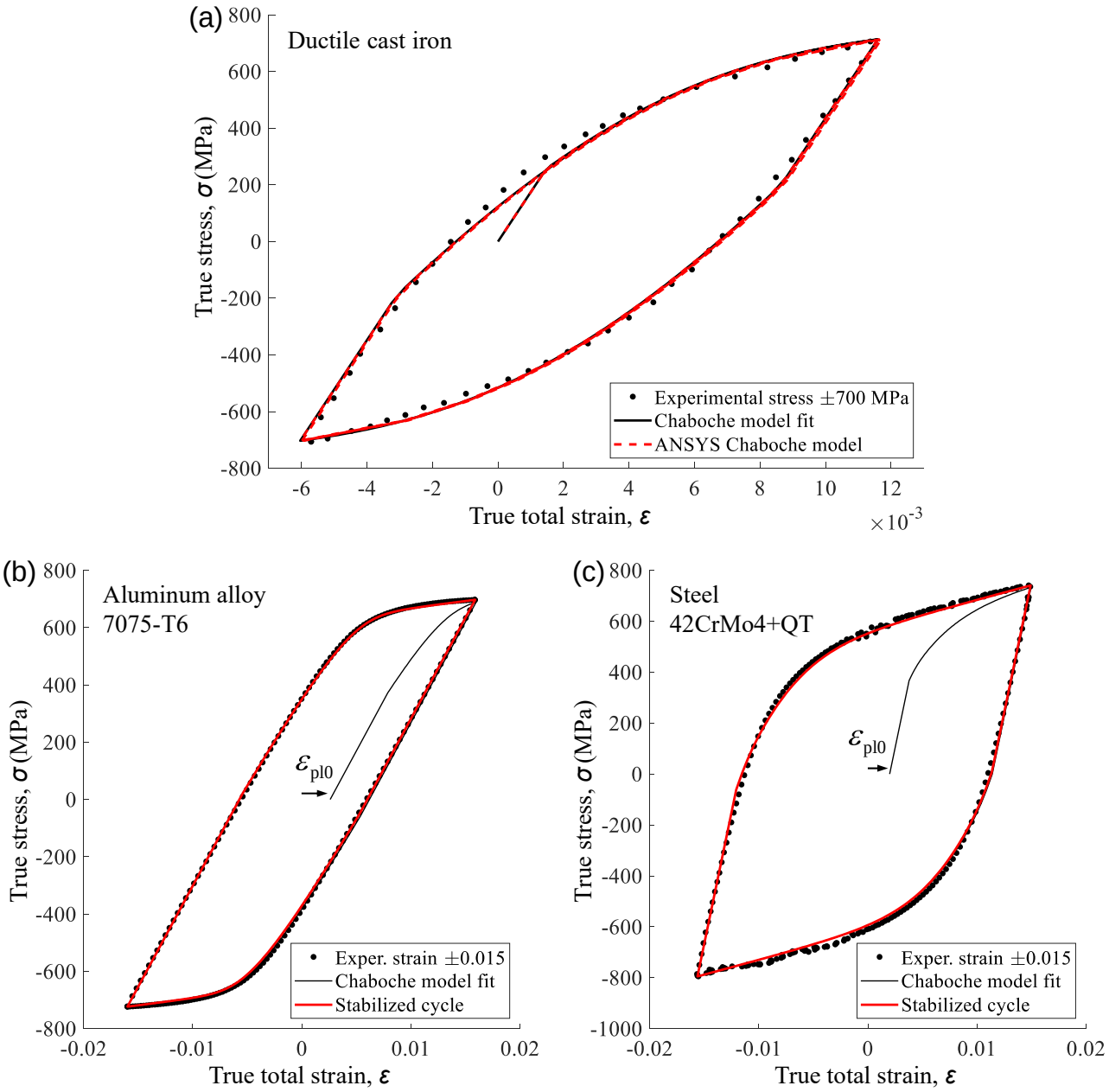

Fig. 7. Chaboche model fit of the largest stabilized cycle for (a) ductile cast iron investigated by Meyer [41]. (b) 7075-T6 aluminum alloy and (c) 42CrMo4+QT steel by Santus et al. [39].

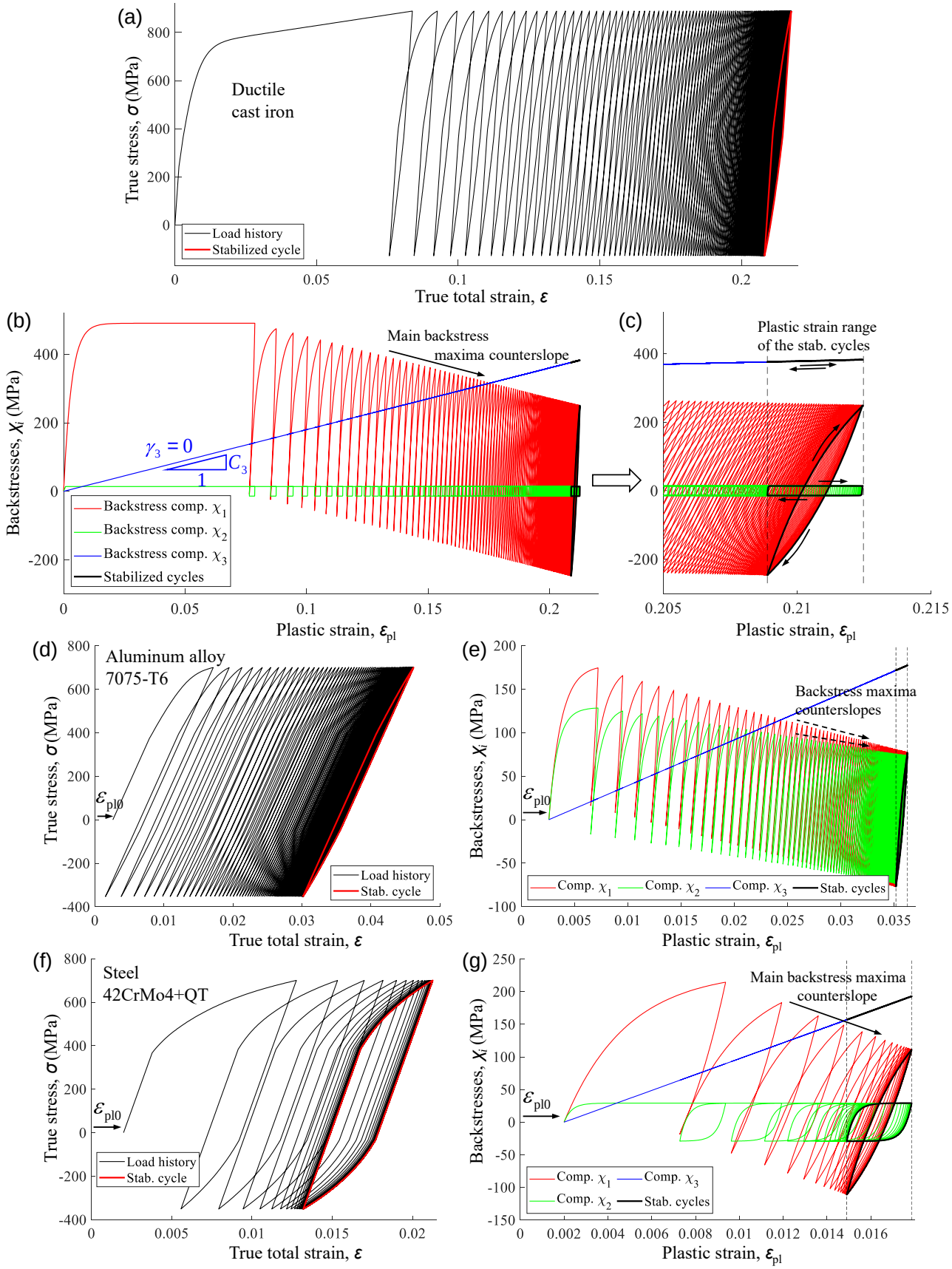

Fig. 8. Ductile cast iron: (a) Ratcheting simulation with stabilization trend; (b) Backstress evolutions and interaction between the first and the third components; (c) Detailed view of the backstress stabilized cycles. 7075-T6 aluminum alloy: (d) Stabilizing ratcheting example; (e) significant

counterslopes of both nonzero-backstress components. 42CrMo4+QT steel: (d) Ratcheting example with evidence of faster stabilization; (f) again counterslope of a single nonzero-backstress component.

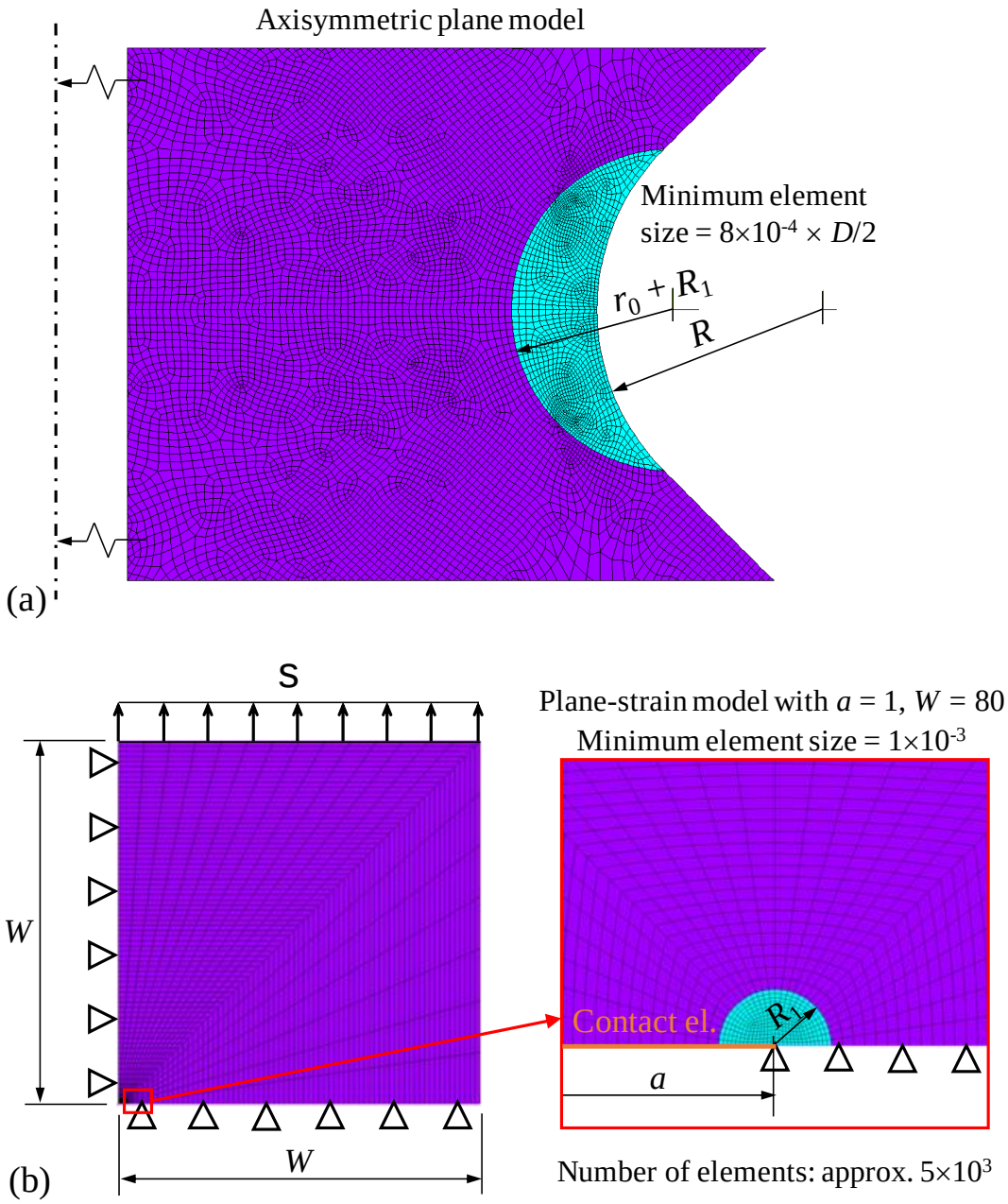

Fig. 9. FE models of (a) notched specimens and (b) fracture mechanics specimens.

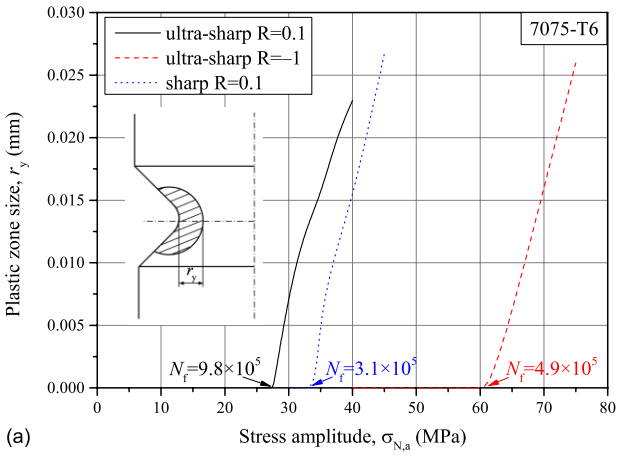
7075-T6
ultra-sharp R=0.1
ultra-sharp R=−1
sharp R=0.1
r_y
N_f=9.8×10^5
N_f=3.1×10^5
N_f=4.9×10^5
Plastic zone size, r_y (mm)
Stress amplitude, $\sigma_{N,a}$ (MPa)

(a)

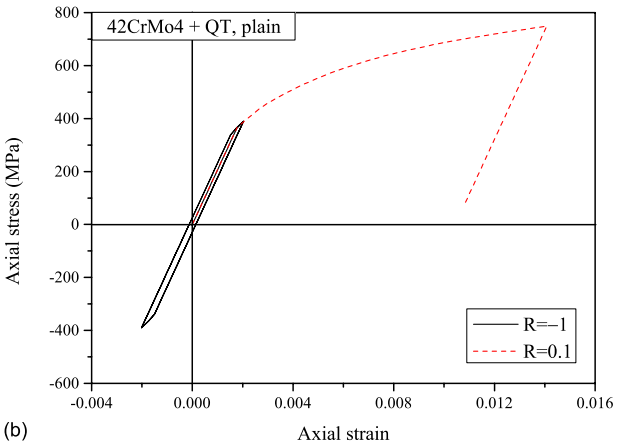
42CrMo4 + QT, plain
R=−1
R=0.1
Axial stress (MPa)
Axial strain

(b)

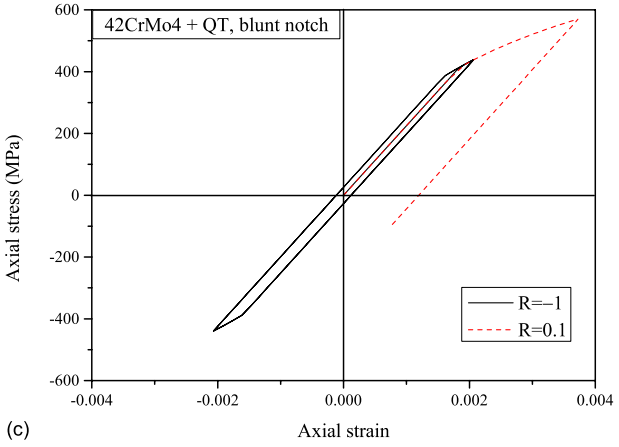
42CrMo4 + QT, blunt notch
R=−1
R=0.1
Axial stress (MPa)
Axial strain

(c)

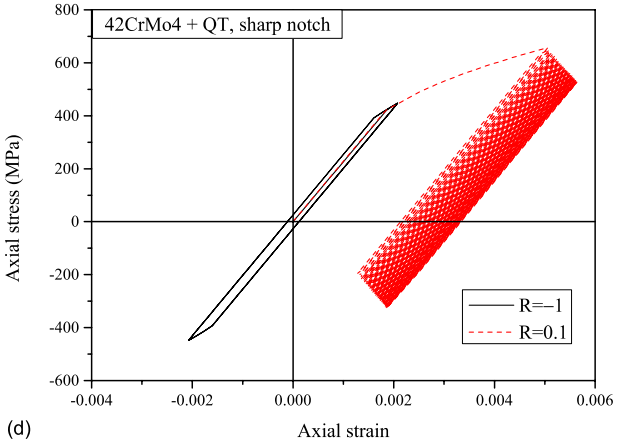
42CrMo4 + QT, sharp notch
R=−1
R=0.1
Axial stress (MPa)
Axial strain

(d)

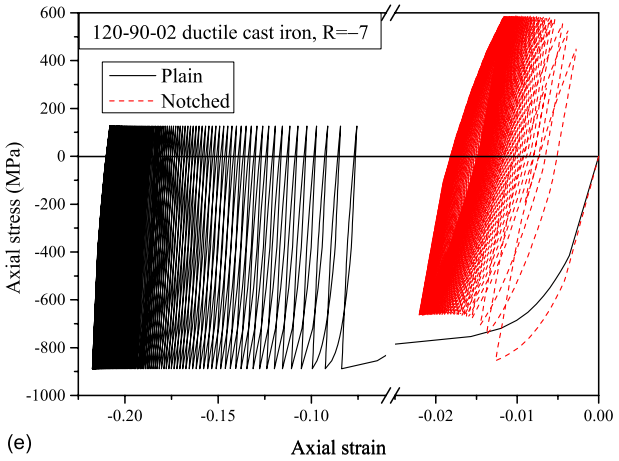
120-90-02 ductile cast iron, R=−7
Plain
Notched
Axial stress (MPa)
Axial strain

(e)

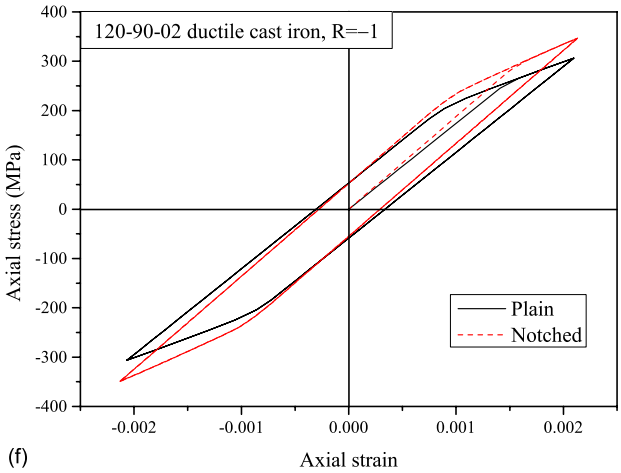
120-90-02 ductile cast iron, R=−1
Plain
Notched
Axial stress (MPa)
Axial strain

(f)

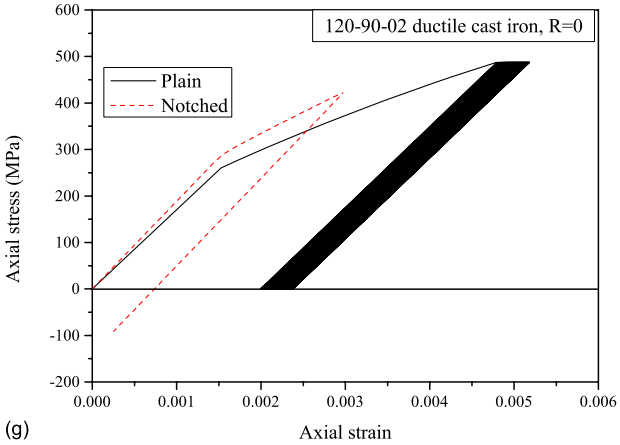
120-90-02 ductile cast iron, R=0
Plain
Notched
Axial stress (MPa)
Axial strain

(g)

Fig. 10. (a) Plastic zone size ahead ultra-sharp and sharp notched specimens of 7075-T6 as a function of the stress amplitude. Evolution of the stress-strain cycle with fatigue life in (b)-(d) 42CrMo4+QT steel and (e)-(g) ductile cast iron at HCF stress amplitudes.

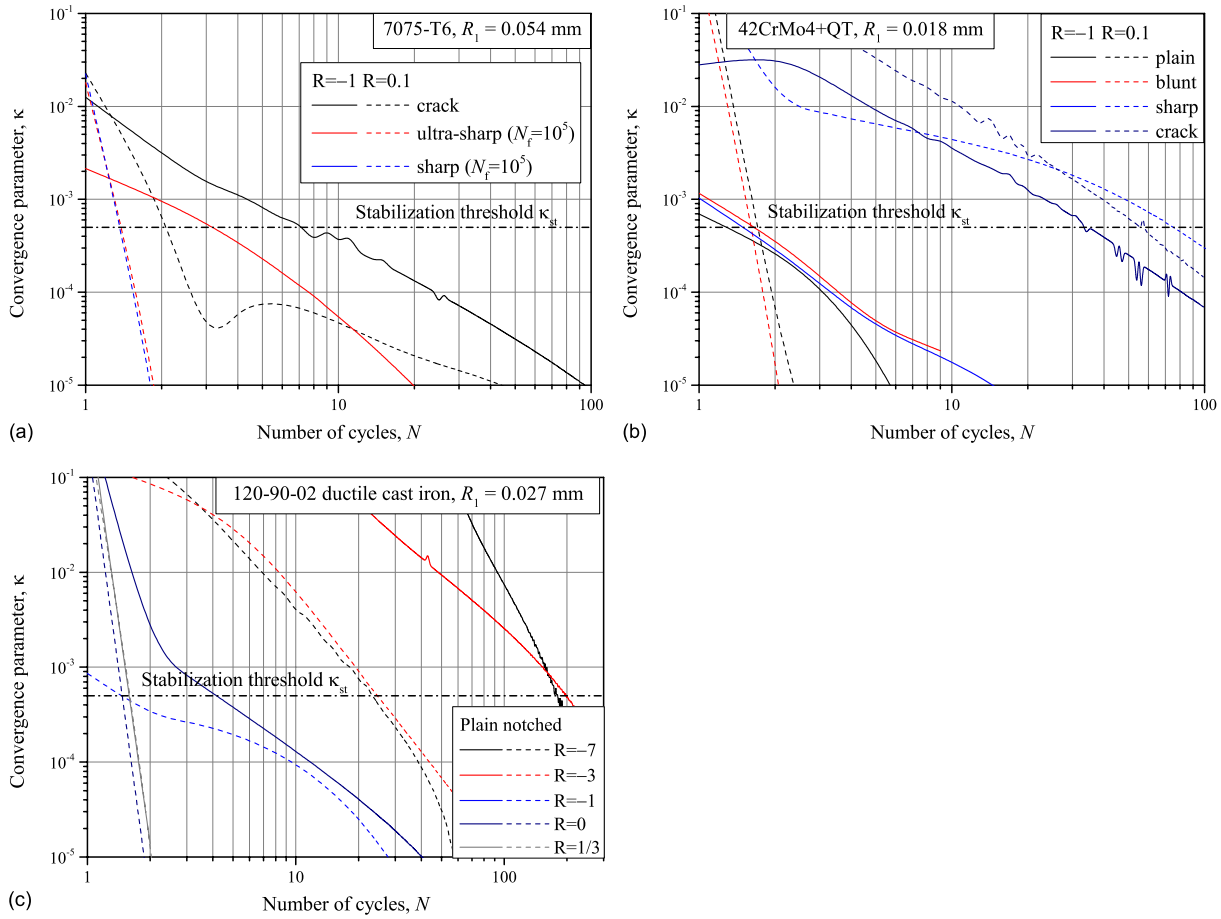

Fig. 11. Convergence criterion for the three investigated materials to estimate the number of cycles at stabilization N_{st}. (a) 7075-T6, (b) 42CrMo4+QT, (c) DCI.

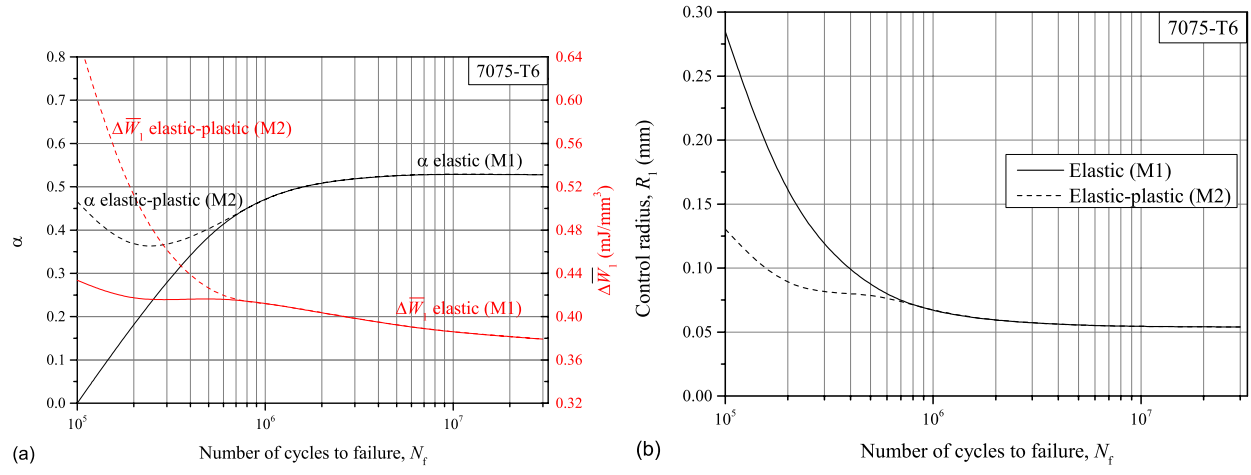

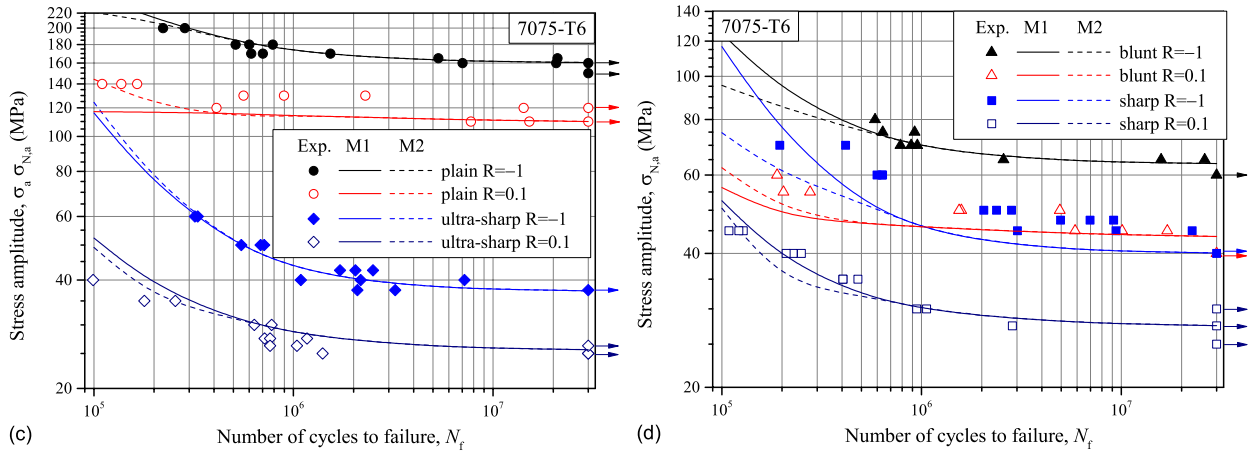

Fig. 12. Fatigue criteria applied to 7075-T6 aluminum alloy. Dependency of (a) criteria material parameters and (b) control radius upon the number of cycles to failure. Comparison of criteria predictions with experimental data (c) used and (d) not-used to calibrate the material parameters. The plastic parameter β is taken independent of N_f and equal to –4.5.

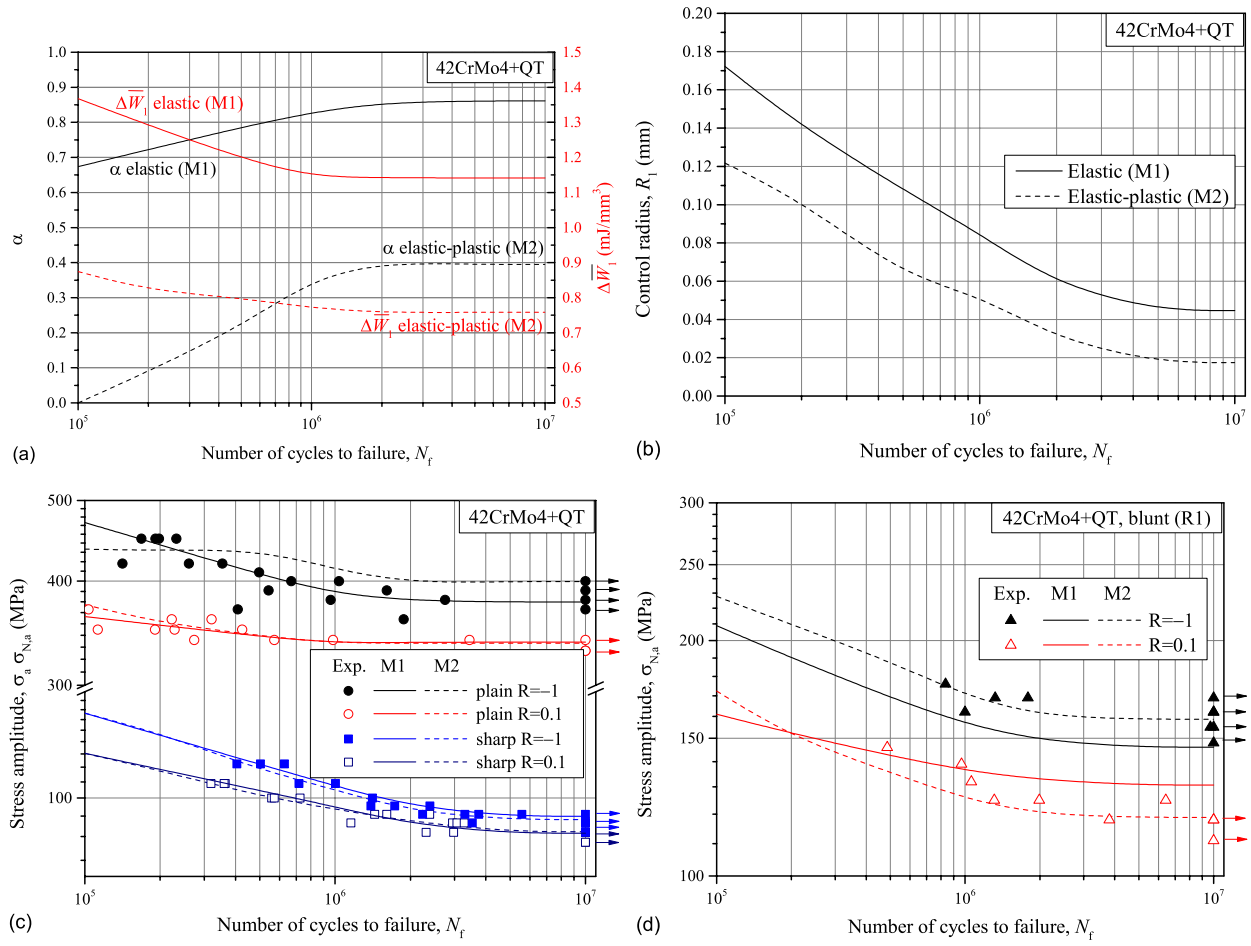

Fig. 13. Fatigue criteria applied to 42CrMo4+QT steel. Dependency of (a) criteria material parameters and (b) control radius upon the number of cycles to failure. Comparison of criteria predictions with

experimental data (c) used and (d) not-used to calibrate the material parameters. The plastic parameter β is taken independent of N_f and equal to –0.0848.

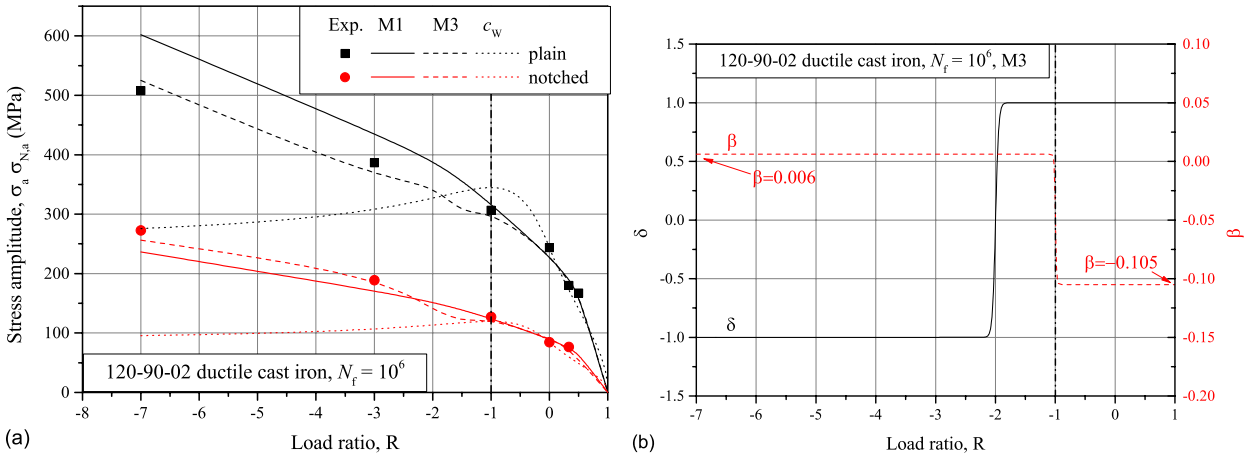

Fig. 14. Fatigue criteria applied to ductile cast iron. (a) Comparison of predictions according to M1, M3 and c_W approach (Eq. (1c)) with experimental data. (b) Dependency of M3 plastic parameters upon load ratio R.

Tables

Table 1. Monotonic tensile properties based on three replicated tests. Standard error corresponds to 1σ uncertainty band.

Material	*E* (GPa)	σ_{YS} (MPa)	σ_U (MPa)	*T.E.* (%)
7075-T6	70.5±0.2	531±7	595±6	10.0±0.7
42CrMo4+QT	206±5.9	727±14	875±15	17.6±2.5
120-90-02 DCI	174	644	1006	9.1
E: Young's modulus, σ_{YS}: 0.2% yield stress, σ_U: ultimate tensile strength, *T.E.*: total elongation				

Table 2. Fatigue crack growth threshold from experiments conducted in [39].

Material	Sample geometry	Load ratio R	ΔK_{th} (MPa $m^{0.5}$)
7075-T6	M(T)	-1	4.2
	C(T)	0.1	2.5
42CrMo4+QT	M(T)	-1	9.1
	C(T)	0.1	7.2

Table 3. Chaboche best-fit coefficients of the investigated metal alloys.

Material	E(GPa)	ν	σ_0(MPa)	C_1 MPa	γ_1	C_2(MPa)	γ_2	C_3(MPa)	γ_3
7075-T6	70.5	0.33	373	153700	865	154700	1201	5270	0
42CrMo4+QT	206	0.30	367	81750	353	83990	2882	12160	0
120-90-02 DCI	174	0.27	243	153000	312	849700	60960	1800	0

Table 4. Best-fit coefficients of the fatigue models of the investigated metal alloys.

Material	N_f	Model	α	$D\overline{W}_1$ (mJ/mm^3)	R_1 (mm)	β	δ
7075-T6	3×10^7	M1	0.529	0.380	0.0539	-	-
		M2	0.529	0.380	0.0539	–4.50	-
42CrMo4+QT	1×10^7	M1	0.861	1.142	0.0447	-	-
		M2	0.395	0.759	0.0175	–0.0848	-
120-90-02 DCI	1×10^6	M1	0.512	0.597	0.0572	-	-
		M3	0.319	0.565	0.0265	b_1=–0.056 b_2=50.1 b_3=50.1 b_4=–0.049	d_1=19.4 d_2=38.8

Table 5a. High-cycle fatigue strength predictions ($N_f = 3\times10^7$) for 7075-T6 according to linear-elastic model M1. The highest absolute errors are marked in bold.

Model	Test	Geometry	R	Exp. σ_a (MPa) / ΔK_{th} (MPa m$^{0.5}$)	St.dev. (MPa)	Estimation	Err. (%)
M1	Self-consistency	Plain	-1	159	5.2	160	0.6
			0.1	116	9.4	110	**–5.2**
		Ultra-sharp (R0.1)	-1	38.2	2.19	37.3	–2.4
			0.1	24.9	1.46	25.6	2.8
	Validation	Blunt (R1)	-1	62.3	2.86	63.6	2.1
			0.1	45.0	2.72	43.7	–2.9
		Sharp (R0.2)	-1	42.0	2.69	40.1	–4.5
			0.1	27.0	1.43	27.5	1.9
		MT	-1	4.2	-	4.30	2.4
		CT	0.1	2.5	-	2.95	**18**
	Max abs. error (%)						18
	RMS error (%)						6.4

Table 5b. High-cycle fatigue strength predictions ($N_f = 3\times10^7$) for 7075-T6 according to elastic-plastic M2 model. For comparison purpose, the errors marked in bold refer to the same estimations indicated in Table 5a.

Model	Test	Geometry	R	Exp. σ_a (MPa) / ΔK_{th} (MPa m$^{0.5}$)	St.dev. (MPa)	Estimation	Err. (%)
M2	Self-consistency	Plain	-1	159	5.2	160	0.6
			0.1	116	9.4	110	**–5.2**
		Ultra-sharp (R0.1)	-1	38.2	2.19	37.3	–2.4
			0.1	24.9	1.46	25.6	2.8
		MT	-1	4.2	-	4.45	6.0
		CT	0.1	2.5	-	2.65	**6.0**
	Validation	Blunt (R1)	-1	62.3	2.86	63.6	2.1
			0.1	45.0	2.72	43.7	–2.9
		Sharp (R0.2)	-1	42.0	2.69	40.1	–4.5
			0.1	27.0	1.43	27.5	1.9
	Max abs. error (%)						6.0

	RMS error (%)	3.9

Table 6a. High-cycle fatigue strength predictions ($N_f = 1\times10^7$) for 42CrMo4+QT according to linear-elastic M1 model. The highest absolute errors are marked in bold.

Model	Test	Geometry	R	Exp. σ_a (MPa) / ΔK_{th} (MPa $m^{0.5}$)	St.dev. (MPa)	Estimation	Err. (%)
M1	Self-consistency	Plain	-1	390	20.7	378	–3.1
			0.1	337	5.3	338	0.3
		Sharp (R0.2)	-1	87.5	2.93	88.8	1.5
			0.1	80.5	2.65	79.5	–1.2
	Validation	Blunt (R1)	-1	163	12.1	146	–**10**
			0.1	119	3.71	131	**10**
		MT	-1	9.1	-	8.3	–8.8
		CT	0.1	7.2	-	7.4	2.8
	Max abs. error (%)						10
	RMS error (%)						6.1

Table 6b. High-cycle fatigue strength predictions ($N_f = 1\times10^7$) for 42CrMo4+QT according to elastic-plastic M2 model. For comparison purpose, the errors marked in bold refer to the same estimations indicated in Table 6a.

Model	Test	Geometry	R	Exp. σ_a (MPa) / ΔK_{th} (MPa $m^{0.5}$)	St.dev. (MPa)	Estimation	Err. (%)
M2	Self-consistency	Plain	-1	390	20.7	400	2.5
			0.1	337	5.30	337	0.0
		Sharp (R0.2)	-1	87.5	2.93	86.9	–0.6
			0.1	80.5	2.65	80.3	–0.3
		MT	-1	9.1	-	9.1	0.2
		CT	0.1	7.2	-	7.0	–3.1
	Validation	Blunt (R1)	-1	163	12.1	159	–**2.7**
			0.1	119	3.71	119	–**0.1**
	Max abs. error (%)						3.1
	RMS error (%)						1.7

Table 7a. High-cycle fatigue strength predictions (N_f = 1×10^6) for 120-90-02 ductile cast iron according to linear-elastic M1 model. The highest absolute errors are marked in bold.

Model	Test	Geometry	R	Exp. σ_a (MPa)	Estimation	Err. (%)
M1	Self-consistency	Plain	-1	306	320	4.6
			0	244	228	–6.6
		Notched	-1	127	125	–1.6
			0	84.5	89.0	5.3
	Validation	Plain	-7	508	629	**24**
			-3	386	448	**16**
			1/3	180	187	3.9
			0.5	167	162	–3.0
		Notched	-7	273	245	–10
			-3	189	175	–7.4
			1/3	76.4	73.0	–4.5
	Max abs. error (%)					24
	RMS error (%)					10

Table 7b. High-cycle fatigue strength predictions (N_f = 1×10^6) for 120-90-02 ductile cast iron according to elastic-plastic M3 model. For comparison purpose, the errors marked in bold refer to the same estimations indicated in Table 7a.

Model	Test	Geometry	R	Exp. σ_a (MPa)	Estimation	Err. (%)
M3	Self-consistency	Plain	-7	508	525	**3.3**
			-3	386	360	–**6.7**
			-1	306	306	0
			0	244	235	–3.7
			1/3	180	185	2.8
		Notched	-7	273	256	–6.2
			-3	189	199	5.3
			-1	127	124	–2.4
			0	84.5	91.4	8.2
			1/3	76.4	74.8	–2.1
	Validation	Plain	0.5	167	169	1.2
	Max abs. error (%)					8.2
	RMS error (%)					4.5